Please cite this article in press as: Jo et al., A natural compound derivative targeting HADHA disrupts mitochondrial homeostasis and suppresses renal cell carcinoma, Molecular Therapy (2026), https://doi.org/10.1016/j.ymthe.2026.10.014

Molecular Therapy
Original Article

A natural compound derivative targeting HADHA disrupts mitochondrial homeostasis and suppresses renal cell carcinoma

Ara Jo,[1,9] Sanjeevram Dhandapani,[1,9] Ziqin Wang,[1,9] Hyeryeon Jung,[1,9] Hongjun Jang,[2] Morgan A. Bailey,[2] Andrew Tran,[1] Brandon Tsai,[3] Jinjae Park,[2] Hyejin Lee,[2] Hye-Jin Park,[1,2] Yoojin Lim,[2] Dolce Feenaghty,[2] Victor M. Moncada,[2] Damu Wu,[4] Keaton Chien,[1] Nancy Chen,[1] Yunsol Jo,[1] Jiazheng Miao,[5] Zhujun Yao,[1] Jihoon Lee,[6] Karthigayan Shanmugasundaram,[6] Gang Greg Wang,[1,4,7] Andrew Armstrong,[7,8] Daniel George,[7,8] David Howell,[1] Jiaoti Huang,[1] Michael C. Fitzgerald,[2] Jiyong Hong,[2] and Jung Wook Park[1,7]

[1]Department of Pathology, Duke University School of Medicine, Durham, NC 27710, USA; [2]Department of Chemistry, Duke University, Durham, NC 27708, USA; [3]Department of Microbiology, Immunology, and Molecular Genetics, University of California, Los Angeles, Los Angeles, CA 90095, USA; [4]Department of Pharmacology and Cancer Biology, Duke University School of Medicine, Durham, NC 27710, USA; [5]Department of Electrical and Computer Engineering, Duke University, Durham, NC 27710, USA; [6]Department of Molecular Medicine, The University of Texas Health Science Center at San Antonio, San Antonio, TX 78229, USA; [7]Duke Cancer Institute Center for Prostate and Urologic Cancer, Durham, NC 27710, USA; [8]Department of Medicine, Division of Medical Oncology, Duke University, Durham NC 27710, USA

Metastatic renal cell carcinoma (RCC) remains a lethal malignancy, and therapeutic resistance to current targeted and immune-based therapies highlights the need for new treatment strategies. Here, we identify C18-epi-brasilibactin A (CBA) as a selective inhibitor of RCC. High-throughput screening of a compound library derived from natural products revealed that CBA potently suppresses RCC cell proliferation, while sparing normal renal epithelial and liver cells. Mechanistically, CBA induces cell-cycle arrest, apoptosis, and DNA damage. Transcriptomic and functional analyses showed that CBA disrupts mitochondrial homeostasis by increasing mitochondrial mass and reactive oxygen species, indicating metabolic stress. Using proteomic approaches, we identified hydroxyacyl-CoA dehydrogenase trifunctional multienzyme complex subunit alpha (HADHA), a key enzyme in mitochondrial fatty acid β-oxidation, as a key functional mediator of CBA. Genetic depletion of HADHA phenocopied CBA effects, inducing ROS accumulation, DNA damage response, apoptosis, and growth inhibition in RCC cells. CBA treatment significantly suppressed RCC xenograft growth, without systemic toxicity. Consistently, HADHA knockdown inhibited tumor progression, whereas HADHA overexpression enhanced tumor growth, supporting a tumor-supportive role for HADHA in RCC. Together, our findings identify HADHA-dependent mitochondrial metabolism as a functional vulnerability in RCC and establish CBA as a candidate therapeutic agent for targeting metabolic dependencies in metastatic RCC.

INTRODUCTION

Renal cell carcinoma (RCC) is the most common type of kidney cancer, accounting for approximately 90% of renal malignancies. It ranks as the 14th most common cancer globally, with over 430,000 new cases diagnosed each year, and has a particularly high incidence in Europe and North America, including an estimated 80,000 new cases annually in the United States alone.[1–3] Although early-stage RCC is often asymptomatic and treatable by surgical resection, with 5-year survival rates above 90% for stage I disease,[4] metastatic RCC or stage IV kidney cancer poses a significant clinical challenge due to its aggressive behavior and poor prognosis.[5] RCC frequently metastasizes to the lungs, lymph nodes, liver, bones, and brain; however, clinical outcomes have improved in the era of contemporary systemic therapy. In patient cohorts stratified by International Metastatic RCC Database Consortium (IMDC) risk criteria, modern immunotherapy-based and combination treatment regimens are associated with distinct survival outcomes across favorable, intermediate, and poor-risk groups.[6,7] Despite these advances, there remains an urgent need for new and more effective therapeutic strategies to further improve outcomes for patients with RCC.

The therapeutic landscape for RCC has evolved substantially over the past two decades.[8] While partial or radical nephrectomy remains the primary curative approach for localized RCC, systemic therapies are the mainstay for RCC.[9] Targeted therapies including VEGF-directed tyrosine kinase inhibitors (TKIs), such as sunitinib, pazopanib, cabozantinib, lenvatinib, and axitinib, alongside immune checkpoint

Received 11 March 2026; accepted 13 October 2026;
https://doi.org/10.1016/j.ymthe.2026.10.014.

[9]These authors contributed equally

Correspondence: Jung Wook Park, Department of Pathology, Duke University School of Medicine, Durham, NC 27710, USA.
E-mail: jungwook.park@duke.edu

 © 2026 The American Society of Gene and Cell Therapy. Published by Elsevier Inc. All rights are reserved, including those for text and data mining, AI training, and similar technologies.

Please cite this article in press as: Jo et al., A natural compound derivative targeting HADHA disrupts mitochondrial homeostasis and suppresses renal cell carcinoma, Molecular Therapy (2026), https://doi.org/10.1016/j.ymthe.2026.10.014

inhibitors like nivolumab, ipilimumab, and pembrolizumab or dual checkpoint blockade now constitute standard first-line treatments.[10] These therapies have improved median overall survival; however, durable responses remain limited to less than 25% of patients. Most patients ultimately develop intrinsic or acquired resistance and treatment-related toxicities, such as fatigue, hypertension, and immune-related adverse events, which frequently compromise quality of life.[11] Moreover, therapeutic efficacy varies across RCC subtypes and patient populations, and predictive biomarkers remain limited.[12] Collectively, these challenges underscore the urgent need for novel therapeutic agents that can overcome resistance, improve selectivity, and minimize toxicity.

Natural products have historically provided a rich source of anticancer therapeutics, with more than a half of clinically approved chemotherapeutic agents derived from or inspired by natural compounds.[13] Actinomycetes constitute a group of Gram-positive bacteria found in terrestrial and marine environments and are prolific producers of bioactive secondary metabolites exhibiting diverse pharmacological activities, including antibiotics and anticancer agents.[14] Notably, doxorubicin and bleomycin, both derived from *Streptomyces* species, are widely used in cancer therapy.[15] The actinomycete *Nocardia brasiliensis* produces brasilibactin A, a siderophore natural product with reported cytotoxicity activity against L1210 and KB cell lines.[16] However, the therapeutic potential, selectivity, and molecular targets of brasilibactin A derivatives in RCC have not been explored.

In this study, we performed a focused screen of natural product-derived small molecules and identified C18-epi-brasilibactin A (CBA) as a potent and selective cytotoxic agent against two currently available metastatic RCC cell lines (Caki-1 and ACHN), while sparing normal renal (HK-2) and liver (HepG2) cells. We demonstrate that CBA suppresses RCC growth *in vitro* and *in vivo* by inducing G2/M cell-cycle arrest, apoptosis, and DNA damage. Mechanistically, CBA disrupts mitochondrial homeostasis, leading to increased mitochondrial mass and reactive oxygen species (ROS) production. Proteomic analysis identifies hydroxyacyl-CoA dehydrogenase trifunctional multienzyme complex subunit alpha (HADHA), a key regulator of mitochondrial fatty acid β-oxidation, as a CBA-interacting protein and a functional mediator of CBA-associated anti-tumor effects. Together, these findings position CBA as a novel therapeutic candidate for RCC and reveal a mitochondrial metabolic vulnerability that may be exploited to overcome current treatment limitations.

RESULT

A natural compound derivative, CBA, inhibits the growth of metastatic RCC cells

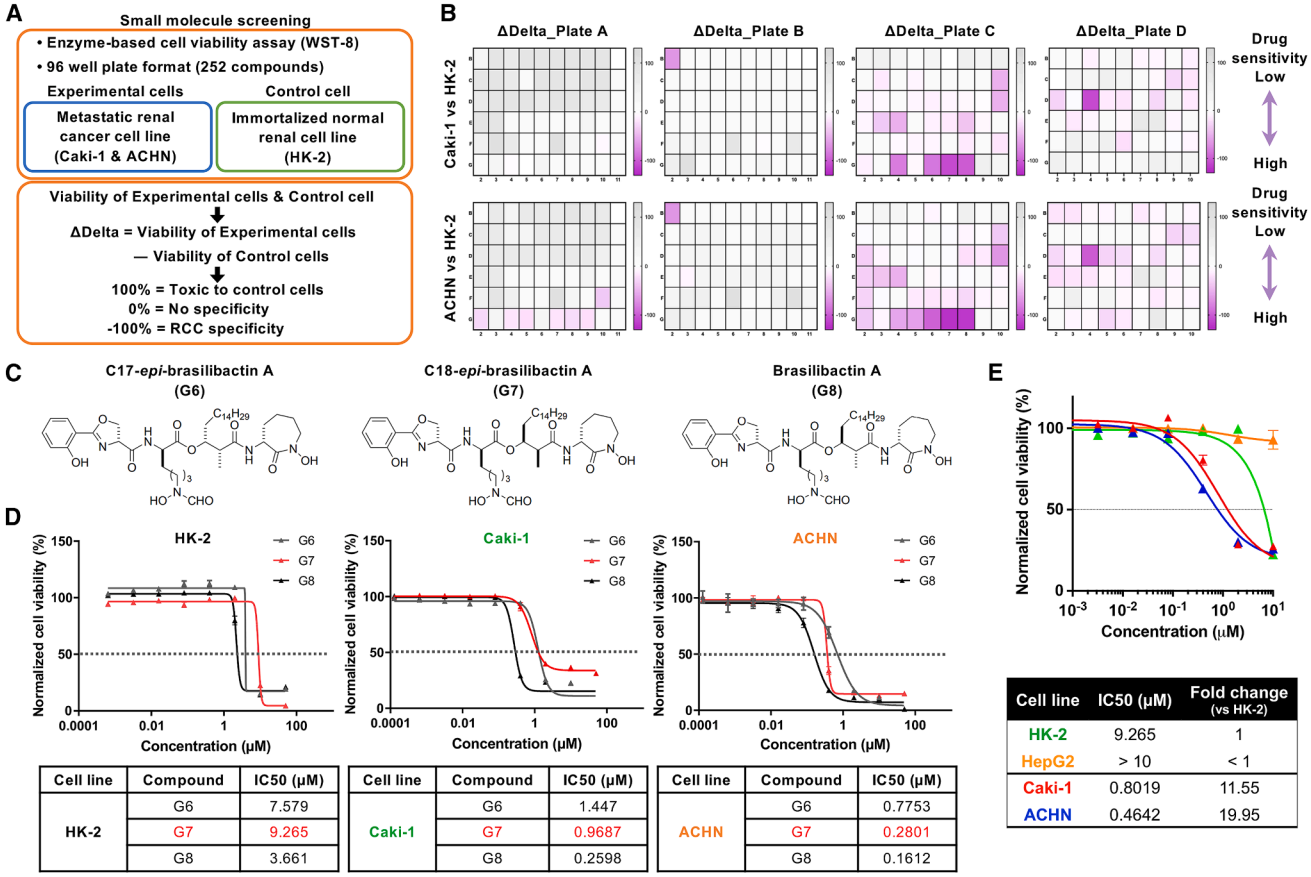
Identifying new vulnerabilities in metastatic RCC is essential for improving therapeutic options. To discover potential anticancer candidates, we performed a screen of 252 small molecules derived from natural compounds in two representative metastatic RCC cell lines, Caki-1 (clear cell RCC [ccRCC]) and ACHN (papillary RCC [pRCC]). In parallel, we evaluated compound toxicity in the immortalized normal renal epithelial cell line HK-2 to identify RCC-selective compounds with inhibitory activity. All compounds were tested at 10 μM for 48 h, and cell viability was measured in a 96-well format (Figure 1A).

To prioritize compounds with RCC-selective activity, we calculated Δ viability scores (Δ viability = RCC viability [%] − HK-2 viability [%]). Several compounds exhibited stronger cytotoxicity toward RCC cells than toward HK-2 cells, suggesting RCC-selective activity (Figures 1B and S1). Among the hits, we identified brasilibactin A (G8) and its derivatives (G6:C17-epi-brasilibactin A and G7:CBA) as leading candidates (Figure 1C). We measured the IC50 (half-maximal inhibitory concentration) of these three compounds (Figure 1D). We selected the G7/CBA compound for our further studies due to its lowest toxicity and highest IC50 in HK-2 cells. Additionally, to evaluate hepatotoxicity, we measured the IC50 of HepG2 cells, a human liver cancer cell line that is widely used in *in vitro* drug toxicity studies.[17] We observed no cytotoxic effect of CBA on HepG2 cells (Figure 1E), which also suggests that CBA has specificity for RCC cells. On the basis of the IC50 value of CBA, concentrations of 1 and 2 μM were selected for downstream mechanistic assays. At these doses, CBA robustly reduced viability in Caki-1 and ACHN cells, while sparing HK-2 cells, confirming its selective activity (Figure S2). These results suggest CBA as a selective and potent inhibitor of RCC cell growth, supporting its mechanistic and preclinical evaluation.

CBA induces cell-cycle arrest and apoptosis in RCC cells

To assess long-term proliferative capacity following CBA exposure, we performed colony formation assays.[18] CBA significantly reduced colony formation in both Caki-1 and ACHN cells after 1- or 2-day treatments, while HK-2 cells showed no significant changes (Figure 2A). We next evaluated CBA effects on cell proliferation. Flow cytometric analysis revealed a pronounced accumulation of Caki-1 and ACHN cells in the G2/M phase after CBA treatment, consistent with G2/M arrest, whereas HK-2 cells exhibited no detectable shift in cell cycle distribution (Figures 2B and S3). Immunoblotting with well-established cell cycle-related biomarkers further supported this phenotype, showing decreased phosphorylation of CDC2 (p-CDC2) and histone H3 (p-HH3), along with changes in cyclin A2, cyclin B1, p21, and phosphorylated RB (p-RB) in RCC cells (Figure 2C). No change in these cell cycle markers was observed in HK-2 cells, confirming the tumor selectivity of CBA. We then investigated whether CBA-induced growth inhibition was accompanied by cell death. Annexin V staining demonstrated a dose-dependent increase in apoptotic Caki-1 and ACHN populations after CBA treatment, while HK-2 cells remained unaffected (Figure 2D). Etoposide served as a positive control and induced apoptosis in both RCC and HK-2 cell lines. Consistent with these results, immunoblotting verified the upregulation of two well-known apoptosis markers, cleaved caspase-3 and cleaved PARP, in CBA-treated RCC cells, with no significant changes in HK-2 cells (Figure 2E). Overall, these findings suggest that CBA selectively induces cell-cycle arrest and

Please cite this article in press as: Jo et al., A natural compound derivative targeting HADHA disrupts mitochondrial homeostasis and suppresses renal cell carcinoma, Molecular Therapy (2026), https://doi.org/10.1016/j.ymthe.2026.10.014



Cell line	Compound	IC50 (μM)
HK-2	G6	7.579
	G7	9.265
	G8	3.661

Cell line	Compound	IC50 (μM)
Caki-1	G6	1.447
	G7	0.9687
	G8	0.2598

Cell line	Compound	IC50 (μM)
ACHN	G6	0.7753
	G7	0.2801
	G8	0.1612

Cell line	IC50 (μM)	Fold change (vs HK-2)
HK-2	9.265	1
HepG2	> 10	< 1
Caki-1	0.8019	11.55
ACHN	0.4642	19.95

Figure 1. CBA specifically inhibits viability in metastatic renal cell carcinoma cells

(A) Schematic of small-molecule screening. A WST-8 assay screened 252 compounds in RCC (Caki-1 and ACHN) and normal renal (HK-2) cells. Differential viability (ΔDelta) was calculated by subtracting HK-2 viability from RCC cell viability. (B) Heatmaps showing ΔDelta values for four screening plates. Darker purple indicates higher RCC-specific sensitivity. (C) Chemical structure of G6 (C17-epi-brasilibactin A), G7 (C18-epi-brasilibactin A/CBA), and G8 (brasilibactin A). (D) Dose-response curves (IC50) for G6, G7, or G8 in HK-2, Caki-1, and ACHN cells. For HK-2 cells, G6: R^2 = 0.8581, 95% CI: 3.848–15.91 μM; G7: R^2 = 0.9217, 95% CI: 5.966–14.79 μM; and G8: R^2 = 0.9394, 95% CI: 2.499–5.359 μM. For Caki-1 cells, G6: R^2 = 0.9481, 95% CI: 1.006–2.099 μM; G7: R^2 = 0.9579, 95% CI: 0.6667–1.408 μM; and G8: R^2 = 0.9395, 95% CI: 0.1754–0.3882 μM. For ACHN cells, G6: R^2 = 0.9776, 95% CI: 0.6048–0.9940 μM; G7: R^2 = 0.9481, 95% CI: 0.1975–0.3982 μM; and G8: R^2 = 0.9667, 95% CI: 0.1194–0.2174 μM. Results are presented as the mean ± standard error. (E) Dose-response curves (IC50) for CBA in HK-2, HepG2, Caki-1, and ACHN cells. IC50 values and fold changes relative to HK-2 are shown in the table. HK-2: R^2 = 0.9217, 95% CI: 5.287–16.23 μM; HepG2: R^2 = 0.3571, 95% CI: ambiguous; Caki-1: R^2 = 0.9452, 95% CI: 0.4959–1.297 μM; ACHN: R^2 = 0.9511, 95% CI: 0.2972–0.7251 μM. Results are presented as the mean ± standard error.

apoptotic cell death in RCC cells, while sparing normal renal epithelial cells.

CBA induces DNA damage and activates p53-dependent stress responses selectively in RCC cells

To elucidate the molecular basis of CBA's anti-tumor activity, we performed mRNA sequencing in Caki-1 and ACHN cells treated with CBA. Principal component analysis (PCA) showed significant transcriptomic changes following CBA treatment (Figure 3A). Gene Ontology and pathway enrichment analyses of differentially expressed genes (DEGs) identified notable activation of the p53 signaling pathway, TNF-α/NF-κB signaling, and G2/M checkpoint regulation, along with reduced Myc target gene expression (Figure 3B). Consistent with these transcriptomic changes, immunoblotting showed increased phosphorylation of p53 (p-p53), upregulation of its downstream effector MDM2, and decreased c-Myc expression, along with reduced phosphorylation of STAT3 (p-STAT3) (Figure 3C). These alterations are consistent with our earlier observations of apoptosis induction and cell-cycle arrest (Figure 2). Given the strong activation of p53, we hypothesized that CBA might induce DNA damage in RCC cells. Immunofluorescence staining showed a significant increase in γH2AX-positive nuclear foci, markers of DNA double-strand breaks, in Caki-1 and ACHN cells treated with CBA but not in HK cells (Figures 3D and 3E). Comet assays further confirmed extensive DNA fragmentation in both RCC lines after CBA treatment, while HK-2 cells showed no detectable comet tail formation. As expected, etoposide caused DNA breaks in HK-2 cells (Figures 3F and 3G). We next assessed

Please cite this article in press as: Jo et al., A natural compound derivative targeting HADHA disrupts mitochondrial homeostasis and suppresses renal cell carcinoma, Molecular Therapy (2026), https://doi.org/10.1016/j.ymthe.2026.10.014

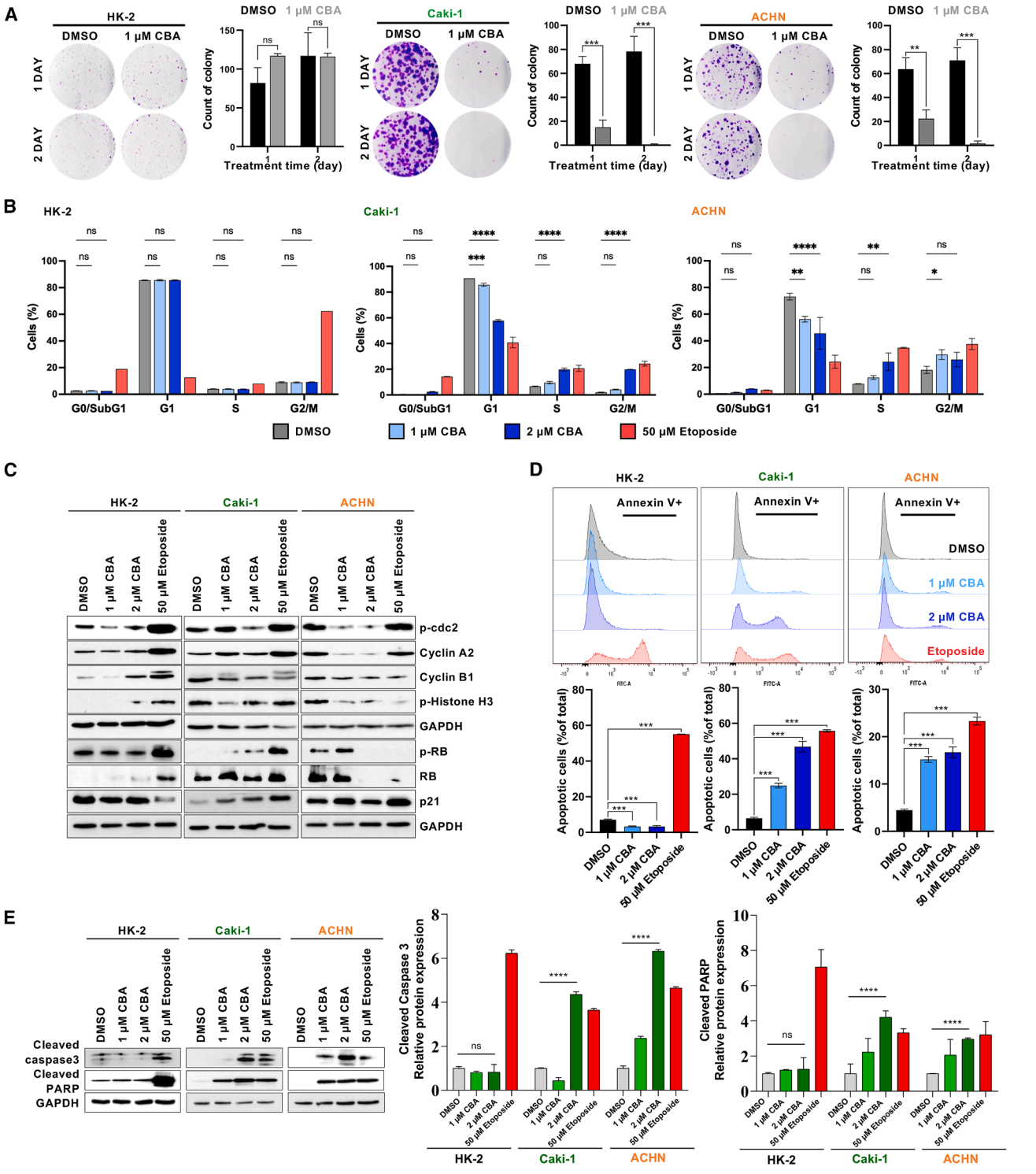


Figure 2. CBA effectively inhibits RCC proliferation by inducing apoptosis and interfering with the RCC cell cycle

(A) Clonogenic survival assays in HK-2, Caki-1, and ACHN cells treated with DMSO or CBA (1 μM) for 48 h. The bar graph represents the count of colonies. (B) Cell cycle analysis by flow cytometry in the treated HK-2, Caki-1, and ACHN cells. (C) Immunoblot of cell cycle proteins (p-CDC2, cyclin A2, cyclin B1, p-HH3, p-RB, RB, and p21) in

(legend continued on next page)

Please cite this article in press as: Jo et al., A natural compound derivative targeting HADHA disrupts mitochondrial homeostasis and suppresses renal cell carcinoma, Molecular Therapy (2026), https://doi.org/10.1016/j.ymthe.2026.10.014

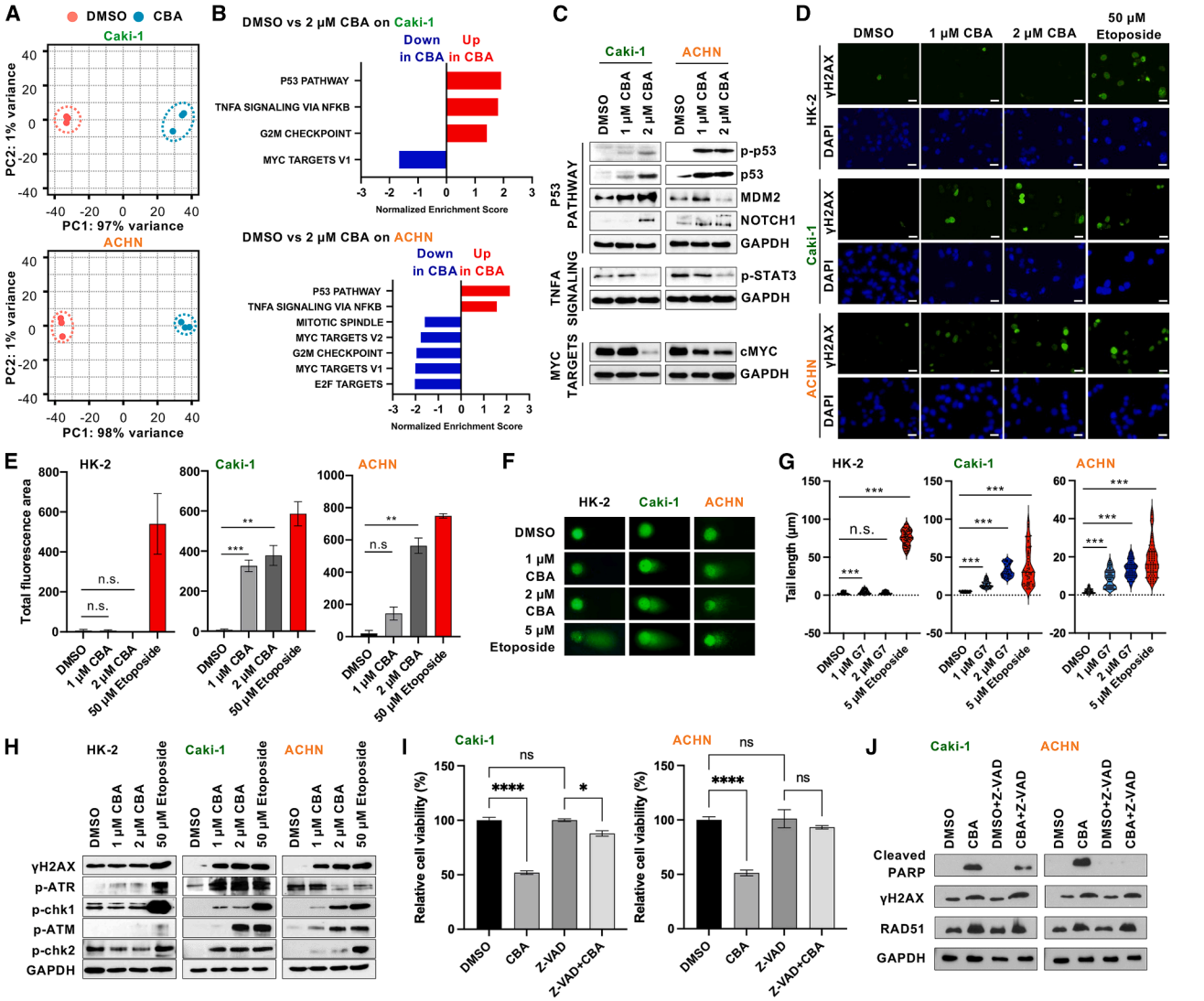


Figure 3. CBA treatment activates a DNA damage response and causes DNA breaks in RCC cells

(A) Principal component analysis (PCA) plots show transcriptomic profiles of Caki-1 and ACHN cells treated with DMSO or CBA. (B) Pathway analysis compares CBA-treated Caki-1 and ACHN cells with DMSO-treated cells, highlighting upregulated and downregulated pathways. (C) Immunoblot analysis shows the protein expression in the p53 pathway (p-p53, p53, MDM2, and NOTCH1), TNF-α signaling (p-STAT3), and Myc targets (c-Myc) in Caki-1 and ACHN cells treated with DMSO or CBA. (D and E) Immunofluorescence shows γH2AX (green, a DNA damage marker) in HK-2, Caki-1, and ACHN cells treated with DMSO, CBA, or etoposide. Nuclei are stained with DAPI (blue). A bar graph quantifies γH2AX foci per nucleus. (F and G) Alkaline comet assay shows DNA fragmentation in HK-2, Caki-1, and ACHN cells treated with DMSO, CBA, or etoposide. A violin plot quantifies comet tail length, indicating DNA break severity. (H) Immunoblot analysis of DNA damage markers (γH2AX, p-ATR, p-Chk1, p-ATM, and p-Chk2) in HK-2, Caki-1, and ACHN cells treated with DMSO, CBA, or etoposide. GAPDH serves as the loading control. All cells were treated with DMSO, CBA (1 or 2 μM), or etoposide (50 μM, positive control). (I) Viability of RCC cells treated with DMSO, z-VAD-FMK, CBA, or z-VAD-FMK plus CBA. (J) Immunoblot analysis of cleaved PARP, γH2AX, and RAD51 in RCC cells treated with z-VAD-FMK, CBA, or z-VAD-FMK plus CBA. GAPDH was used as the loading control. All results are presented as the mean ± SD. Significance is indicated by $^{*}p < 0.05$, $^{***}p < 0.001$, and $^{****}p < 0.0001$ vs. DMSO. ns: Non-significant.

activation of DNA damage response pathways. CBA deregulated both single-strand and double-strand break signaling pathways, as evidenced by DNA damage repair pathway-associated protein markers such as increased ATR and phosphorylated Chk1 (p-Chk1), as well as ATM and phosphorylated Chk2 (p-Chk2), in RCC cells (Figure 3H). None of these responses were observed in

HK-2, Caki-1, and ACHN cells treated with DMSO or CBA. (D) Apoptosis analysis by Annexin V staining using flow cytometry in the treated HK-2, Caki-1, and ACHN cells. (E) Immunoblot of apoptotic markers (cleaved caspase-3 and cleaved PARP) in treated cells. All cells were treated with DMSO, CBA (1 or 2 μM), or etoposide (50 μM, positive control). All results are presented as the mean ± SD. Significance is indicated by $^{*}p < 0.05$, $^{**}p < 0.01$, $^{***}p < 0.001$, and $^{****}p < 0.0001$ vs. DMSO. ns: Non-significant.

Please cite this article in press as: Jo et al., A natural compound derivative targeting HADHA disrupts mitochondrial homeostasis and suppresses renal cell carcinoma, Molecular Therapy (2026), https://doi.org/10.1016/j.ymthe.2026.10.014

HK-2 cells, indicating the selective anticancer potential of CBA in RCC cells.

Because DNA damage and DNA damage response can arise as secondary consequences of apoptosis, we investigated whether CBA-induced DNA damage response depends on caspase-mediated apoptotic execution. To establish conditions for caspase inhibition, we evaluated the cytotoxicity and functional activity of the well-established pan-caspase inhibitor z-VAD-FMK.[19] z-VAD-FMK (25 μM) exhibited no cytotoxicity and effectively inhibited etoposide-induced apoptosis (Figure S4). z-VAD-FMK nearly restored viability in CBA-treated ACHN cells, whereas partial recovery was observed in CBA-treated Caki-1 cells, indicating that caspase-dependent apoptosis contributes to the cytotoxic effects of CBA (Figure 3I).

Immunoblot analysis demonstrated that z-VAD-FMK alone did not induce cleaved PARP, whereas CBA treatment markedly increased cleaved PARP expression in both Caki-1 and ACHN cells. In ACHN cells, z-VAD-FMK almost completely suppressed CBA-induced cleaved PARP, whereas in Caki-1 cells, PARP cleavage was substantially reduced but remained detectable, indicating effective, but incomplete, inhibition of CBA-induced apoptosis (Figure 3J). Despite caspase inhibition, CBA-induced γH2AX expression was maintained in both cell lines. Similarly, RAD51, another marker of DNA damage response,[20] remained elevated following CBA treatment in the presence of z-VAD-FMK (Figure 3J).

Collectively, our findings demonstrate that CBA induces both DNA damage response signaling and apoptosis in RCC cells. Although inhibition of caspase activity attenuated CBA-induced cytotoxicity and suppressed apoptotic marker expression, the persistence of γH2AX and RAD51 induction indicates that DNA damage response activation is not merely a downstream consequence of caspase-dependent apoptosis. Rather, these findings suggest that CBA-induced DNA damage response signaling occurs upstream of, or in parallel with, apoptotic execution.

CBA treatment deregulates mitochondrial genes and disrupts mitochondrial homeostasis

To further elucidate the mechanisms underlying CBA-induced growth inhibition, apoptosis, and DNA damage above, we examined transcriptional pathways affected by CBA treatment. Gene Ontology analyses revealed significant dysregulation of genes associated with mitochondrial function in both ACHN and Caki-1 cells, along with enrichment of genes involved in the negative regulation of VEGF production and mitochondrial-related pathways (Figure 4A). Notably, CBA treatment led to a coordinated suppression of mitochondrial-associated genes associated with oxidative phosphorylation, mitochondrial antioxidant regulators, fatty acid metabolism, mitochondrial protein folding, and quality control pathways (Figure 4B). These changes suggest that CBA may disrupt mitochondrial function and metabolic homeostasis, potentially contributing to the cytotoxic responses observed in RCC cells. Given the pivotal role of mitochondrial metabolism in apoptosis, we focused on changes in mitochondrial homeostasis induced by CBA. To evaluate mitochondrial abundance in RCC cells, we used the mitochondrial membrane dye MitoTracker[21] to quantify mitochondrial mass. CBA treatment resulted in a dose-dependent increase in mitochondrial content in both Caki-1 and ACHN cells, with no significant changes observed in HK-2 cells (Figure 4C). To further validate changes in mitochondrial content, we performed immunofluorescence staining for TOM20, which is a key component of the mitochondrial outer membrane translocase complex essential for importing nuclear-encoded proteins.[22] We observed a marked increase in TOM20 signal intensity in both RCC cell lines following CBA treatment (Figure 4D), which aligns with the MitoTracker results.

To determine whether the changes above reflected functional mitochondrial stress, we measured ROS, a hallmark of mitochondrial oxidative stress. CBA treatment increased ROS levels in RCC cells in a dose-dependent manner (Figure 4E), indicating disruption of mitochondrial redox homeostasis. Notably, CBA-induced ROS accumulation was maintained in the presence of z-VAD-FMK (Figure 4F), suggesting that oxidative stress occurs independent of caspase-dependent apoptosis. We next examined whether CBA-induced mitochondrial dysfunction was accompanied by changes in proteins regulating mitochondrial dynamics. DRP1 is a key regulator of mitochondrial fission,[23] and phosphorylation of DRP1 at Ser616 promotes fission.[24] In contrast, MFN1 regulates outer mitochondrial membrane fusion,[25] whereas OPA1 controls inner mitochondrial membrane fusion and cristae organization.[26] Immunoblot analysis showed that CBA increased total DRP1 and p-DRP1 Ser616 levels, and these changes were maintained in the presence of z-VAD-FMK (Figure 4G). CBA also decreased MFN1 expression, while increasing OPA1 expression, with similar changes observed in the z-VAD-FMK plus CBA group. In contrast, z-VAD-FMK alone had minimal effects on these mitochondrial homeostasis markers (Figure 4G). These findings indicate that CBA-induced mitochondrial stress and remodeling are maintained despite inhibition of apoptosis.

Collectively, these data suggest that CBA perturbs mitochondrial homeostasis by altering mitochondrial gene programs, increasing mitochondrial mass and ROS, and modulating mitochondrial dynamics-associated proteins in RCC cells. The persistence of these mitochondrial changes following caspase inhibition suggests that mitochondrial dysfunction represents an upstream event in the cellular response to CBA, rather than a secondary consequence of apoptotic execution.

CBA treatment suppresses the growth in RCC xenografts without causing systemic toxicity

To evaluate the translational potential of CBA *in vivo*, we established xenograft models using Caki-1 and ACHN cells in immunodeficient NOD scid gamma (NSG) mice. Once tumors became measurable, mice received intraperitoneal (i.p.) administration of CBA (50 mg/kg). CBA treatment significantly inhibited tumor growth in both models, resulting in a significant reduction in tumor volume and weight compared with vehicle-treated controls (Figures 5A, 5B,

Please cite this article in press as: Jo et al., A natural compound derivative targeting HADHA disrupts mitochondrial homeostasis and suppresses renal cell carcinoma, Molecular Therapy (2026), https://doi.org/10.1016/j.ymthe.2026.10.014

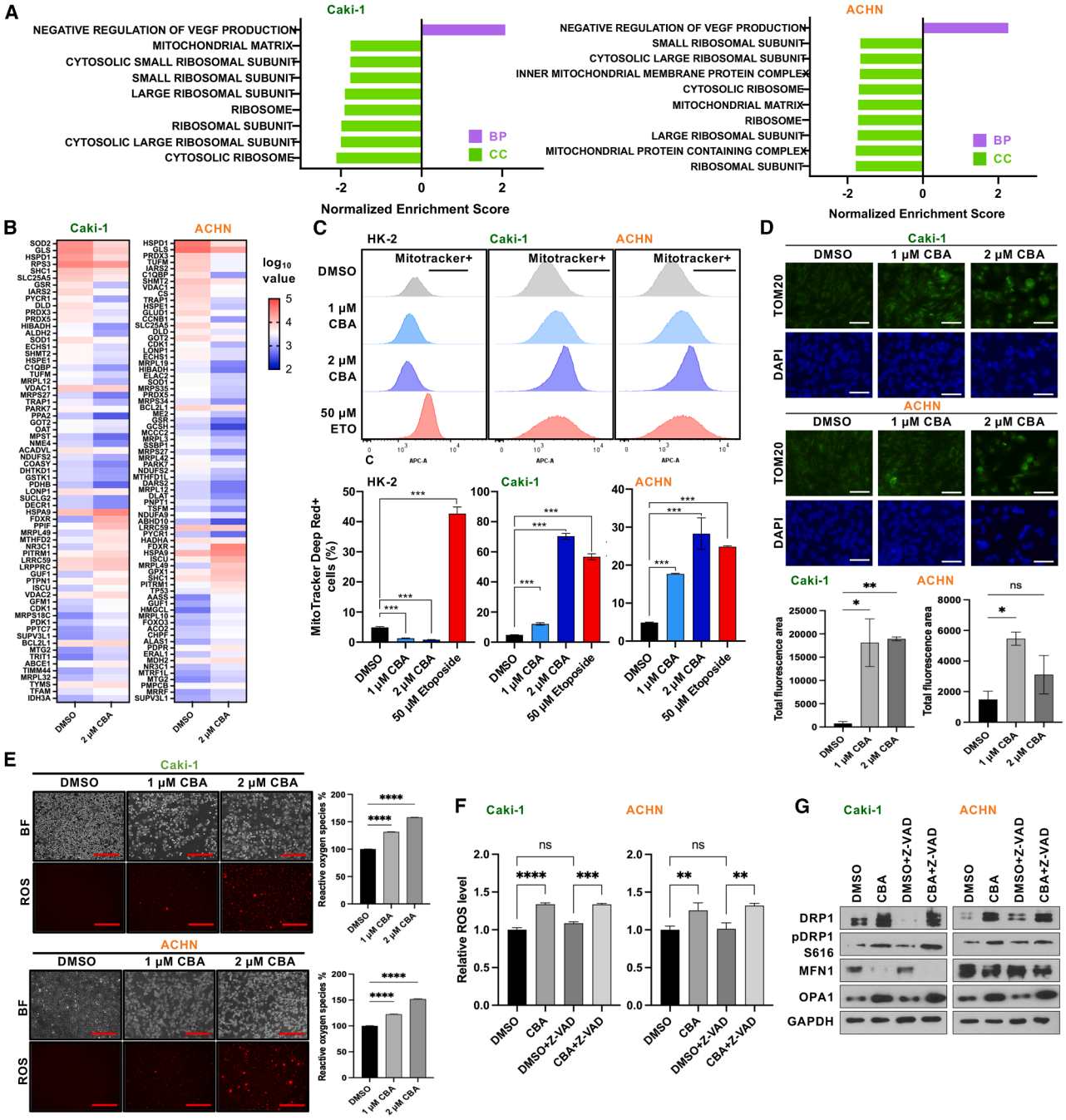
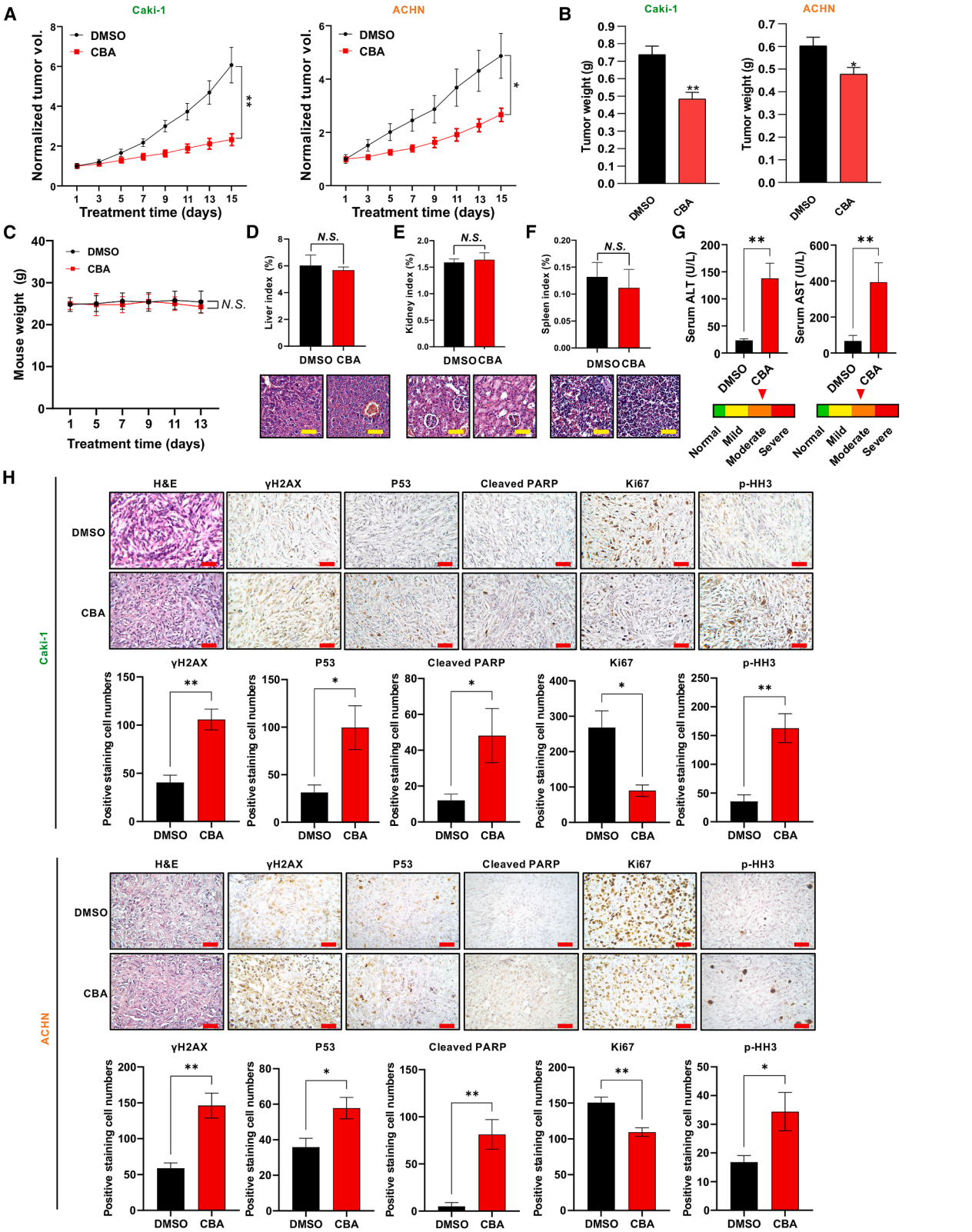


Figure 4. CBA treatment causes mitochondrial dysfunction

(A) Gene Ontology analysis of biological process and cellular components from Caki-1 and ACHN cells treated with CBA. BP, biological process; CC, cellular components. (B) A heatmap shows differential gene expression related to mitochondrial genes in Caki-1 and ACHN cells. (C) Flow cytometric analysis using MitoTracker Red was performed to assess mitochondrial mass in Caki-1 and ACHN cells following treatment with DMSO, CBA (1 or 2 μM), or etoposide (50 μM, as a positive control). The bar graph shows the quantification of MitoTracker Red fluorescence intensity. (D) Immunofluorescence staining of TOM20 and DAPI in Caki-1 and ACHN cells treated with DMSO or CBA (1 or 2 μM). The bar graph shows the TOM20 intensity. (E) ROS staining detected ROS levels in ACHN and Caki-1 cells treated with DMSO and CBA (1 or 2 μM). The bar graph represents the level of ROS release. Scale bars: 20 μm. (F) Intracellular ROS levels in Caki-1 and ACHN cells treated with DMSO, z-VAD-FMK, CBA, or z-VAD-FMK plus CBA. ROS levels were measured using an ROS-sensitive fluorescent probe and are presented as relative fluorescence intensity. (G) Immunoblot analysis of mitochondrial homeostasis-associated proteins in Caki-1 and ACHN cells treated with DMSO, z-VAD-FMK, CBA, or z-VAD-FMK plus CBA. GAPDH was used as the loading control. All results are presented as the mean ± SD. Significance is indicated by $*p < 0.05$, $**p < 0.01$, $***p < 0.001$, and $****p < 0.0001$ vs. DMSO. ns: Non-significant.

Please cite this article in press as: Jo et al., A natural compound derivative targeting HADHA disrupts mitochondrial homeostasis and suppresses renal cell carcinoma, Molecular Therapy (2026), https://doi.org/10.1016/j.ymthe.2026.10.014



(legend on next page)

Please cite this article in press as: Jo et al., A natural compound derivative targeting HADHA disrupts mitochondrial homeostasis and suppresses renal cell carcinoma, Molecular Therapy (2026), https://doi.org/10.1016/j.ymthe.2026.10.014

and S5A). To assess the systemic safety of CBA, we monitored body weight and performed organ toxicity evaluations throughout treatment. No significant changes in body weight, kidney index, spleen index, and liver index were observed following CBA treatment. Histological analysis of the liver, kidney, and spleen tissue showed no significant abnormalities and no sign of fibrosis (Figures 5C–5F and S5B). Complete blood count (CBC) and chemistry assessment of blood samples indicated normal cell parameters despite moderately elevated alanine aminotransferase (ALT) and aspartate aminotransferase (AST) levels, suggesting moderate liver toxicity (Figures S5C and 5G). These findings suggest that CBA treatment does not result in widespread systemic toxicity, except for moderate hepatotoxicity, under the tested conditions. To investigate the molecular mechanisms underlying tumor inhibition, we examined tumor tissues for markers of DNA damage, cell-cycle arrest, and apoptosis. Immunohistochemistry (IHC) and immunoblotting revealed that γH2AX and p53 (DNA damage response markers) were significantly elevated in the CBA-treated group (Figure 5H). CBA also increased the number of cleaved PARP-positive apoptotic cells, while the number of Ki67-positive proliferative cells decreased significantly. Additionally, mitotic cells positive for p-HH3 increased, suggesting cell-cycle arrest at mitosis (Figure 5H).

Collectively, our findings demonstrate that CBA treatment effectively suppresses tumor growth in RCC xenograft models by inducing DNA damage, apoptosis, and cell-cycle arrest, with no acute toxicity. These preclinical results position CBA as a promising therapeutic agent for RCC.

HADHA mediates the cellular effects of CBA treatment in RCC cells

Because the protein targets of CBA-associated cellular effects had not been defined, we applied two complementary proteomic approaches—stability of proteins from rates of oxidation (SPROX)[27] and thermal proteome profiling (TPP)[28]—to identify candidate CBA-associated proteins. These analyses revealed several putative CBA-associated proteins, among which HADHA, CSTF2, RPS19, and PGM1 were consistently identified in both RCC cell lines but not in HK-2 cells (Figures 6A and S6). We examined whether these candidate proteins contributed to RCC cell growth. Inhibiting the expression of CSTF2, RPS19, or PGM1 did not affect viability in RCC cells, whereas HADHA depletion significantly reduced RCC cell viability (Figure S7). Given our earlier findings of CBA-associated mitochondrial disruption (Figure 4), we prioritized HADHA, a key enzyme in mitochondrial fatty acid β-oxidation,[29] for further functional validation.

To further validate the interaction between CBA and HADHA, we performed *in silico* molecular docking to compare CBA binding to trimetazidine dihydrochloride (TMZ), a known HADHA inhibitor.[30] While TMZ bound to HADHA with a predicted energy of −3.0 kcal/mol, CBA exhibited substantially stronger affinity at −8.03 kcal/mol (Figure S8). The docking model indicates that CBA engages overlapping residues with TMZ but forms more extensive interactions, consistent with enhanced binding affinity.

Furthermore, we performed complementary stability-based target-engagement assays. Cellular thermal shift assay (CETSA) demonstrated that CBA increased the thermal stability of HADHA in RCC cells, consistent with cellular target engagement (Figure S9A). We next purified HADHA from 293T cells overexpressing HADHA (Figure S9B) and performed a differential scanning fluorimetry (thermal shift) assay. CBA shifted the HADHA melting curve toward higher temperatures compared with vehicle control (Figure S9C), resulting in an increased melting temperature (Tm) and a positive ΔTm (Figures S9D and S9E). We also confirmed the increased thermal stability of purified HADHA, using an immunoblot assay (Figure S9F). Collectively, these complementary cellular and purified-protein assays support the interaction between CBA and HADHA.

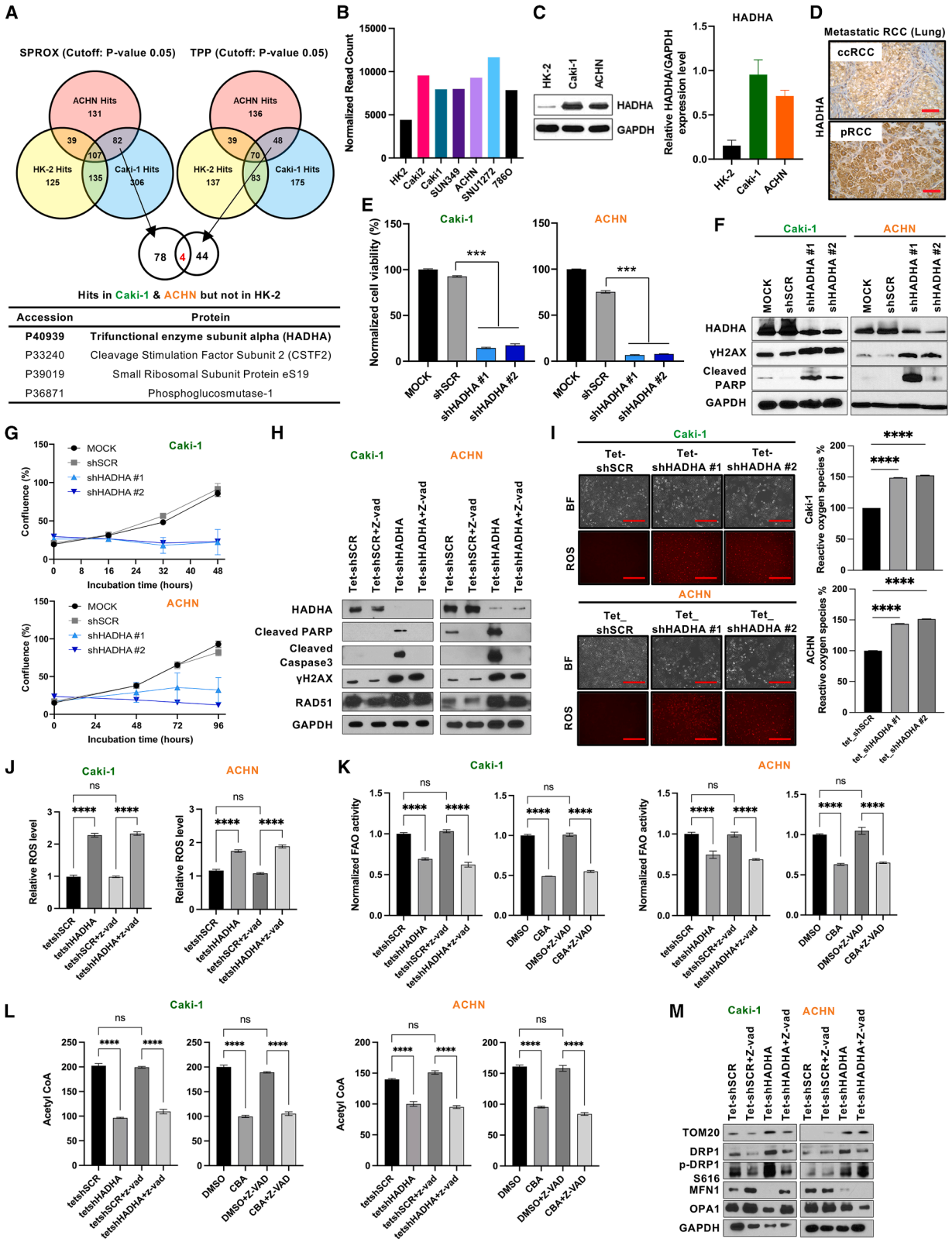
To determine baseline HADHA expression across preclinical renal carcinoma models, we analyzed RNA sequencing (RNA-seq) profiles from multiple RCC cell lines. HADHA transcripts were significantly elevated compared with the immortalized normal renal epithelial line HK-2, with the highest levels observed in Caki-1 and SNU-1272 (Figure 6B). Western blotting confirmed this pattern, showing markedly increased HADHA protein abundance in Caki-1 and ACHN cells relative to HK-2 cells, with densitometry indicating the strongest expression in Caki-1 followed by ACHN (Figure 6C). We also found that HADHA is significantly expressed in metastatic RCC specimens (12 ccRCC and 2 pRCC samples) (Figures 6D and S10). These data support that substantial upregulation of HADHA in RCC may contribute to tumor progression.

To assess the breadth of CBA activity across genetically diverse RCC models, we examined HADHA expression and CBA sensitivity in two additional RCC cell lines, 786-O and RCC4. Both cell lines expressed detectable but lower levels of HADHA than Caki-1 and ACHN cell lines (Figure S11A). Consistent with this observation, CBA inhibited the viability of both 786-O and RCC4 cells, although with higher IC50 values than those observed in Caki-1 and ACHN cells (Figure S11B). These data extend the anti-RCC activity of

Figure 5. CBA treatment inhibited the growth of RCC xenografts

(A) Tumor growth curves of Caki-1 and ACHN xenografts in mice treated with DMSO or CBA. (B) Bar graphs of tumor weights from Caki-1 and ACHN xenografts. (C) Mouse body weight was monitored throughout the treatment period to assess overall toxicity. (D–F) The bar graphs show the liver, kidney, and spleen indices from the DMSO- and CBA-treated groups. Histological analysis using H&E staining of organ sections from DMSO- and CBA-treated mice to evaluate tissue morphology. (G) The bar graph shows the quantification of serum ALT and AST levels in DMSO- and CBA-treated mice, together with an indication of the liver toxicity range. (H) Immunohistochemistry (IHC) of Caki-1 and ACHN xenograft tumor tissues, analyzing markers of γH2AX, p53, cleaved PARP, Ki67, and p-HH3. The bar graphs show the quantification of cells with positive staining. Scale bars: 100 μm. All results are presented as the mean ± SD. Significance is indicated by $^{*}p < 0.05$, and $^{**}p < 0.01$ vs. DMSO. N.S.: Non-significant.

Please cite this article in press as: Jo et al., A natural compound derivative targeting HADHA disrupts mitochondrial homeostasis and suppresses renal cell carcinoma, Molecular Therapy (2026), https://doi.org/10.1016/j.ymthe.2026.10.014



(legend on next page)

Please cite this article in press as: Jo et al., A natural compound derivative targeting HADHA disrupts mitochondrial homeostasis and suppresses renal cell carcinoma, Molecular Therapy (2026), https://doi.org/10.1016/j.ymthe.2026.10.014

CBA to additional RCC models and support a positive association between HADHA expression and cellular response to CBA.

We asked whether HADHA inhibition recapitulates the cellular consequences of CBA exposure. Short hairpin RNA (shRNA)-mediated HADHA knockdown (shHADHA) significantly decreased cell viability in both RCC lines (Figure 6E) and increased γH2AX and cleaved PARP levels (Figure 6F). HADHA depletion also strongly hindered cell proliferation, while mock and scrambled controls reached nearly 100% confluence. HADHA-knockdown cultures remained sparsely populated, with minimal confluence gain at 48 h (Caki-1) and 72 h (ACHN). Phase-contrast imaging and quantitative mask analysis confirmed the substantially reduced density of shHADHA cells (Figures 6G and S12). To further understand HADHA-associated DNA damage response and apoptotic phenotypes, we used doxycycline (Dox)-inducible shRNA targeting HADHA (tet-shHADHA) in RCC cells and evaluated the effect of caspase inhibition with z-VAD-FMK. Immunoblot analysis confirmed efficient HADHA depletion in tet-shHADHA cells (Figure 6H). The increased cleaved caspase-3 or cleaved PARP by loss of HADHA (tet-shHADHA) was decreased in the presence of z-VAD-FMK (tet-shHADHA + Z-VAD), confirming effective inhibition of apoptosis. In contrast, γH2AX and RAD51 remained elevated in tet-shHADHA cells regardless of z-VAD-FMK treatment (Figure 6H), indicating that HADHA depletion-induced DNA damage response signaling occurs independently of apoptosis.

We next investigated the metabolic consequences of HADHA loss. HADHA loss significantly increased ROS levels (Figure 6I), consistent with the CBA-induced ROS (Figure 4). Importantly, z-VAD-FMK did not attenuate ROS accumulation in HADHA-depleted cells (Figure 6J), indicating that ROS accumulate independently of apoptosis.

To determine whether HADHA loss impaired mitochondrial metabolic function, we measured fatty acid oxidation (FAO) activity and acetyl-CoA levels. Both FAO activity and acetyl-CoA levels were significantly reduced in tet-shHADHA cells compared with tet-shSCR control, and these reductions persisted in the presence of z-VAD-FMK. In contrast, z-VAD-FMK alone had no significant effect on either FAO activity or acetyl-CoA levels. We also found that CBA significantly decreased FAO activity and acetyl-CoA levels regardless of z-VAD-FMK (Figures 6K and 6L). These findings demonstrate that HADHA depletion impairs mitochondrial fatty acid metabolism and support a functional interaction between CBA and HADHA.

Consistent with the metabolic changes described above, HADHA depletion also altered mitochondrial homeostasis proteins. TOM20 levels increased after HADHA depletion, suggesting altered mitochondrial abundance or outer mitochondrial membrane abundance. Mitochondrial fusion proteins, OPA1 and MFN1, were reduced, whereas the fission proteins, DRP1 and phospho-DRP1 (Ser616), were increased after HADHA depletion. Although z-VAD-FMK partially attenuated some of these changes, particularly in Caki-1 cells, the overall differences between tet-shSCR and tet-shHADHA cells remained evident regardless of caspase inhibition, indicating persistent mitochondrial remodeling after HADHA depletion (Figure 6M). Notably, OPA1 regulation diverged between chemical inhibition and HADHA depletion, which may reflect acute pharmacologic stress versus chronic metabolic effect.

Our findings demonstrate that genetic depletion of HADHA phenocopies the major cellular effects of CBA treatment, impairing FAO activity, acetyl-CoA production, mitochondrial remodeling, and oxidative stress and inducing activation of the DNA damage response and apoptosis. The persistence of mitochondrial dysfunction, ROS accumulation, and DNA damage response following caspase inhibition supports a model in which HADHA loss initiates metabolic and genotoxic stress upstream of, or in parallel with, apoptosis. Together, these findings identify HADHA as a key functional mediator of the anti-tumor activity of CBA in RCC cells.

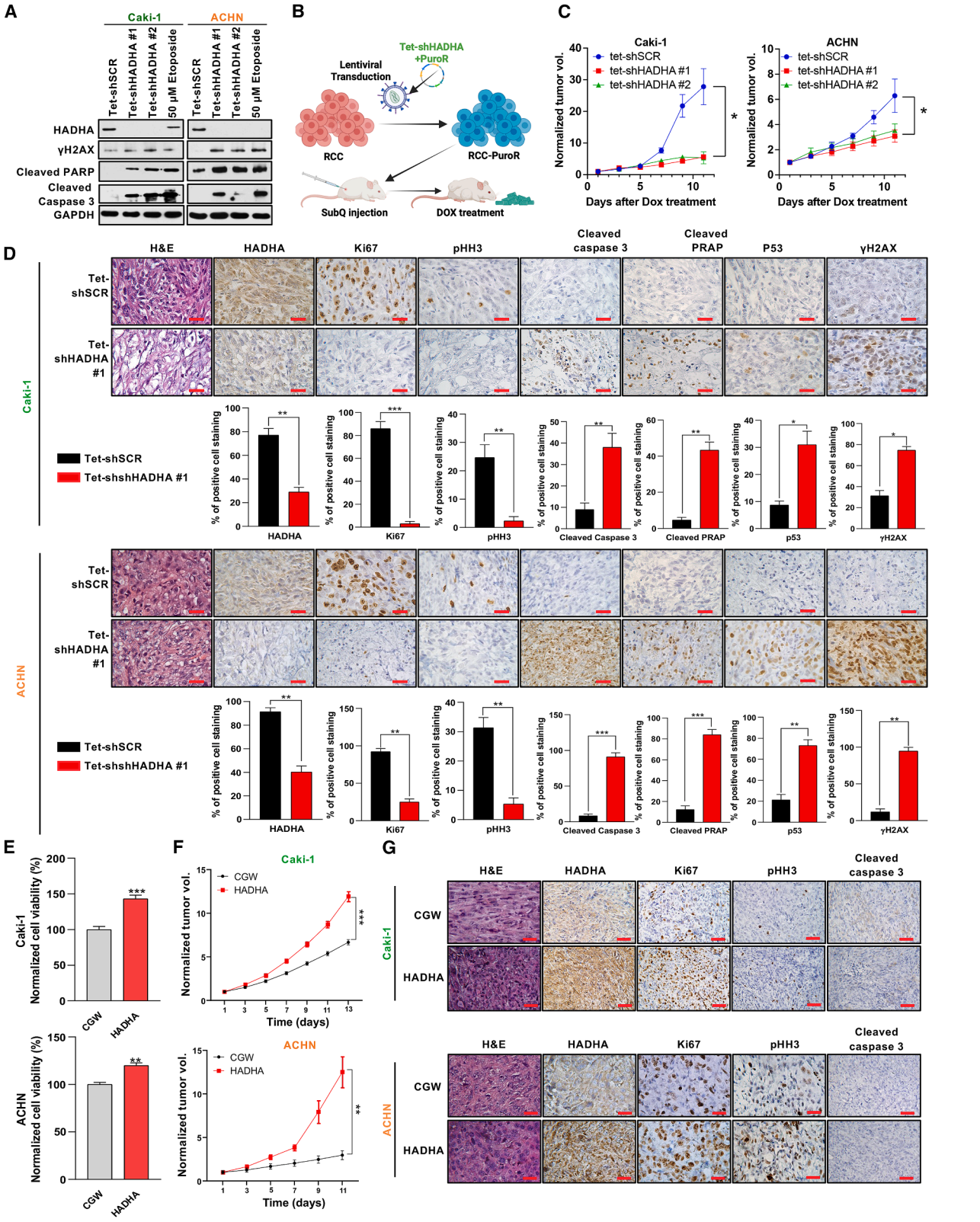
HADHA supports RCC cell survival and tumor growth

Having shown that HADHA depletion phenocopies several cellular effects of CBA, we next examined whether HADHA itself possesses tumor-promoting properties *in vivo*. We generated Dox-inducible HADHA knockdown lines (tet-shHADHA) and confirmed that Dox-induced depletion of HADHA increased γH2AX, cleaved PARP, and cleaved caspase-3 in both cell lines (Figure 7A), consistent with the phenotypes observed with constitutive shHADHA (Figure 6F).

Figure 6. HADHA loss inhibits RCC growth by inducing DNA damage and ROS, mimicking CBA treatment

(A) Venn diagram illustrating overlapping phosphoproteins in Caki-1 and ACHN cells treated with CBA. (B) The bar graph shows the mRNA expression levels of HADHA across various RCC cell lines. (C) Immunoblot analysis of HADHA protein levels in RCC cell lines, accompanied by a bar graph quantifying protein expression. (D) HADHA expression in representative RCC specimens. (E) Cell proliferation assay quantifying the inhibitory effect of HADHA knockdown on Caki-1 and ACHN cell growth. (F) Immunoblot of HADHA, γH2AX, and cleaved PARP in Caki-1 and ACHN cells after shRNA-mediated HADHA knockdown. (G) Quantitation of live-cell imaging analysis using Incucyte over 48 h following HADHA knockdown in Caki-1 and ACHN cells. (H) Immunoblot analysis of HADHA, cleaved PARP, cleaved caspase-3, γH2AX, and RAD51 in tet-shSCR, tet-shSCR plus z-VAD-FMK, tet-shHADHA, and tet-shHADHA plus z-VAD-FMK cells. GAPDH was used as the loading control. (I) ROS staining to measure ROS levels in Caki-1 and ACHN cells following HADHA knockdown, with the bar graphs quantifying ROS release. Scale bars: 100 μm. (J) Quantification of intracellular ROS levels in tet-shSCR, tet-shSCR plus z-VAD-FMK, tet-shHADHA, and tet-shHADHA plus z-VAD-FMK cells. (K) Fatty acid oxidation activity in tet-shSCR, tet-shSCR plus z-VAD-FMK, tet-shHADHA, and tet-shHADHA plus z-VAD-FMK cells. (L) Acetyl-CoA levels in tet-shSCR, tet-shSCR plus z-VAD-FMK, tet-shHADHA, and tet-shHADHA plus z-VAD-FMK cells. (M) Immunoblot analysis of TOM20, OPA1, DRP1, phospho-DRP1 Ser616, and MFN1 in tet-shSCR, tet-shSCR plus z-VAD-FMK, tet-shHADHA, and tet-shHADHA plus z-VAD-FMK cells. GAPDH was used as the loading control. All results are presented as the mean ± SD. Significance is indicated by $^{***}p < 0.001$ and $^{****}p < 0.0001$ vs. DMSO. ns: Non-significant.

Please cite this article in press as: Jo et al., A natural compound derivative targeting HADHA disrupts mitochondrial homeostasis and suppresses renal cell carcinoma, Molecular Therapy (2026), https://doi.org/10.1016/j.ymthe.2026.10.014



(legend on next page)

Please cite this article in press as: Jo et al., A natural compound derivative targeting HADHA disrupts mitochondrial homeostasis and suppresses renal cell carcinoma, Molecular Therapy (2026), https://doi.org/10.1016/j.ymthe.2026.10.014

Mice bearing tet-shHADHA Caki-1 or ACHN xenografts were fed Dox chow to induce shRNA expression (Figure 7B). HADHA depletion significantly inhibited tumor growth in both models (Figures 7C and S13A). Histopathologic analysis revealed striking morphological alterations following HADHA knockdown. tet-shSCR control xenografts displayed densely packed cells with abundant eosinophilic cytoplasm, whereas HADHA loss induced marked cytoplasmic clearing, vacuolization, and a reduction in eosinophilia. These changes were more pronounced in Caki-1 tumors, consistent with their ccRCC cell phenotype characterized by high lipid and glycogen contents compared with the pRCC-ACHN line. Overall, HADHA-depleted tumors shifted from vividly eosinophilic to pale, vacuolated morphologies. Immunohistochemical staining further showed that HADHA loss decreased the proliferation markers Ki67 and p-HH3, while increasing cleaved caspase-3, cleaved PARP, p53, and γH2AX, indicating enhanced apoptosis and DNA damage (Figure 7D).

To further test the oncogenic role of HADHA, we overexpressed HADHA in Caki-1 and ACHN cells. HADHA overexpression significantly increased normalized cell viability relative to a vector control (CGW) (Figure 7E). In xenograft assays, HADHA-overexpressing tumors exhibited accelerated growth and substantially larger volumes throughout the study in both models (Figures 7F and S13B). Histopathologic analysis demonstrated densely packed, highly eosinophilic tumor cells with vivid purple-pink cytoplasm, while IHC revealed strong HADHA expression accompanied by increased Ki67 and p-HH3 and reduced cleaved caspase-3 (Figures 7G and S14).

Together, these data demonstrate that HADHA promotes RCC cell proliferation, suppresses apoptosis, and drives aggressive tumor growth. Combined with our earlier findings, they position HADHA-associated mitochondrial metabolism as a functional vulnerability and compelling therapeutic target in RCC cells.

DISCUSSION

In this study, we identified CBA as a selective inhibitor of metastatic RCC that preferentially suppressed RCC cells, while sparing normal renal cells. CBA induced G2/M arrest, apoptosis, and DNA damage, while disrupting mitochondrial homeostasis, increasing ROS, and impairing FAO activity and acetyl-CoA production, indicating mitochondrial metabolic dysfunction, rather than simple changes in mitochondrial marker expression. Consistent with these *in vitro* findings, CBA effectively suppressed RCC xenograft growth without overt systemic toxicity, supporting its therapeutic potential.

A major finding of this study is the identification of HADHA as a key functional mediator of CBA-associated effects. Proteomic analyses, CETSA, and thermal shift assays supported HADHA as a potential CBA-interacting protein. CBA increased the Tm of purified HADHA, indicating ligand-induced stabilization. Importantly, genetic HADHA depletion phenocopied the major effects of CBA, including impaired FAO, reduced acetyl-CoA production, mitochondrial remodeling, ROS accumulation, DNA damage response activation, apoptosis, and growth inhibition. Together, these findings identify HADHA-dependent mitochondrial fatty acid metabolism as a functional metabolic vulnerability in the RCC models examined, while avoiding overstatement that HADHA has been definitively established as the direct molecular target of CBA. Future studies may need to apply quantitative direct-binding affinity measurements such as surface plasmon resonance and bio-layer interferometry to further determine physical interactions between HADHA protein and CBA compound, as well as profiling the binding kinetics and binding affinity.

Our data further suggest that mitochondrial metabolic disruption precedes or occurs in parallel with DNA damage and apoptosis. Although z-VAD-FMK rescued CBA-induced cell death and reduced apoptotic markers, CBA-induced ROS accumulation, DNA damage response activation, impaired FAO, reduced acetyl-CoA levels, and mitochondrial remodeling persisted under caspase inhibition. Similar findings were observed following HADHA depletion. These results suggest that the disruption of HADHA-associated mitochondrial metabolism may promote oxidative stress and DNA damage, thereby leading to apoptotic cell death, rather than representing a secondary consequence of apoptosis. In addition to its role in mitochondrial fatty acid β-oxidation, HADHA has also been implicated in cardiolipin remodeling through monolysocardiolipin acyltransferase activity. Although the present study did not directly assess cardiolipin or monolysocardiolipin species to measure HADHA cardiolipin-remodeling function (MLCLAT), altered cardiolipin remodeling may represent an additional mechanism linking CBA-associated HADHA perturbation to mitochondrial membrane stress, ROS accumulation, and apoptosis. Future lipidomic analyses will be needed to determine whether disruption of HADHA-mediated cardiolipin remodeling contributes to the mitochondrial stress induced by CBA treatment or HADHA depletion.

Our findings also support a context-dependent pro-tumorigenic role of HADHA in RCC. HADHA depletion suppressed tumor growth, whereas HADHA overexpression enhanced proliferation and xenograft progression (Figure 7). Although previous studies have

Figure 7. HADHA supports RCC cell survival and tumor growth

(A) Immunoblot analysis of HADHA, γH2AX, cleaved PARP, and cleaved caspase-3 in Caki-1 and ACHN cells following tet-shRNA-mediated HADHA knockdown. (B) Schematic of the inducible HADHA knockdown strategy in RCC xenografts, outlining the experimental design. (C) Tumor growth curves of Caki-1 and ACHN xenografts with or without HADHA knockdown. (D) H&E and IHC analyses of Caki-1 and ACHN xenograft tumor tissues stained for HADHA, Ki67, p-HH3, cleaved caspase-3, cleaved PARP, p53, and γH2AX. The bar graphs show the quantification of positive-staining cells. (E) Viability analysis of HADHA-overexpressing Caki-1 and ACHN cells. (F) Tumor growth curves of Caki-1 and ACHN xenografts with or without HADHA overexpression. (G) H&E and IHC images of xenograft tissues stained for HADHA, Ki67, p-HH3, and cleaved caspase-3. Scale bars: 100 μm. All results are presented as the mean ± SD. Significance is indicated by $^{*}p < 0.05$, $^{**}p < 0.01$, and $^{***}p < 0.001$ vs. DMSO.

Please cite this article in press as: Jo et al., A natural compound derivative targeting HADHA disrupts mitochondrial homeostasis and suppresses renal cell carcinoma, Molecular Therapy (2026), https://doi.org/10.1016/j.ymthe.2026.10.014

reported tumor-suppressive functions of HADHA in certain cancers,[31] these apparently conflicting observations likely reflect differences in tumor subtype, metabolic state, or dependence on FAO. RCC is metabolically heterogeneous, and this diversity may influence CBA sensitivity. Although RCC is frequently associated with glycolytic reprogramming,[32] the primary models used in this study, Caki-1 and ACHN, display relatively oxidative metabolic features that may increase their reliance on HADHA-dependent FAO. Consistent with this hypothesis, both CBA treatment and HADHA depletion reduced FAO activity and acetyl-CoA levels, supporting a functional link between mitochondrial fatty acid metabolism and CBA sensitivity. To broaden the analysis, we examined two additional RCC cell lines, 786-O and RCC4, which are VHL-deficient ccRCC models reported to exhibit glycolysis-associated metabolic features.[33] Both cell lines expressed lower levels of HADHA than Caki-1 and ACHN and displayed higher IC50 values for CBA, suggesting that CBA sensitivity may vary with metabolic state and HADHA expression. However, because we did not perform OCR (oxygen consumption rate)/ECAR (extracellular acidification rate)-based metabolic flux analyses under our experimental conditions, we avoided metabolically classifying these models directly. Future studies using metabolically stratified RCC models will be important to identify the tumor subsets most dependent on HADHA-mediated mitochondrial metabolism and therefore most likely to benefit from CBA-based therapy.

Compared with current RCC therapies, including TKIs, immune checkpoint inhibitors, and mTOR inhibitors, CBA exhibits a distinct mechanism of action by simultaneously disrupting mitochondrial fatty acid metabolism, inducing oxidative stress and DNA damage, and triggering apoptosis. This multifaceted mechanism may be particularly effective in metabolically oxidative RCC subsets and further highlights the therapeutic potential of natural product-derived compounds.

Several limitations should be acknowledged. RCC remains metabolically and histologically heterogeneous, and additional studies using patient-derived models, organoids, and metastatic specimens are needed to define the broader applicability of CBA. Moreover, our *in vivo* studies were performed in immunodeficient mice, precluding assessment of immune-mediated effects. Although preliminary toxicity studies showed no overt systemic toxicity, comprehensive toxicological and pharmacokinetic analyses, together with medicinal chemistry optimization, will be required before clinical translation. Finally, the efficacy of CBA in established tumors and in combination with current RCC therapies warrants further investigation.

In summary, our findings identify CBA as a selective suppressor of RCC growth and establish HADHA-dependent mitochondrial metabolism as a functional metabolic vulnerability in RCC. By linking CBA-mediated HADHA engagement to impaired FAO, reduced acetyl-CoA production, oxidative stress, activation of the DNA damage response, and apoptosis, this study provides a mechanistic framework for how disruption of mitochondrial metabolism suppresses RCC progression. Collectively, these findings support the continued development of CBA and related natural product derivatives as therapeutic candidates for metabolically vulnerable subsets of RCC.

MATERIALS AND METHODS

Chemicals and materials

Human metastatic renal cancer cell lines (Caki-1 and ACHN) and an immortalized normal renal cell line (HK-2) were purchased from the cell culture facility at Duke University (NC, USA). Dulbecco's modified Eagle's medium (DMEM) and 1% penicillin/streptomycin solution were obtained from Corning Life Sciences, NY, USA. Fetal bovine serum (FBS) and keratinocyte-SFM (serum-free media) were purchased from Gibco, NY, USA. The p-CDC2 (#4539), cyclin A2 (#91500), cyclin B1 (#12231), p-HH3 (#53348), p-RB (#8516), p21(#2947), DNA damage Ab sampler kit (#9947), γH2AX (#9718), cleaved caspase-3 (#9661), cleaved PARP (#94885), p-p53 (#9286), MDM2 (#86934), NOTCH1 (#3608), p-STAT3 (#9134), HIF-1α (#36169), VHL (#68547), Ferroptosis Ab sampler kit (#29650), EZH2 (#5246), and NOTCH2 (#5732) antibodies were purchased from Cell Signaling Technology (MA, USA). RB (#ab181616) and c-Myc (#ab32072) were purchased from Abcam (MA, USA). p53 (#21891) and PTTG1 (#18040) were purchased from Proteintech (IL, USA). GAPDH (#sc-47724) was purchased from Santacruz (CA, USA).

Cell viability and clonogenic assays

Caki-1 and ACHN cells were cultured in DMEM with 10% FBS and 1% penicillin/streptomycin, while HK-2 cells were grown in keratinocyte-SFM, all maintained at 37°C in a 5% CO_2 humidified atmosphere. Cell viability was assessed in 96-well plates seeded at 10,000 cells/well, using the water-soluble tetrazolium (WST-8) assay (S7764, Selleckchem, TX, USA). Cells were treated with 10 μM synthetic compounds for 24 h, followed by the addition of 10 μL WST-8 solution per well and a 2-h incubation. The solution absorbance was measured at 460 nm, using a microplate reader. A colony formation assay was performed by seeding 500 cells per well in 6-well plates. After 24 h, the cells were treated with 1 μM CBA for 14 days. To fix the colonies, the cells were treated with 4% paraformaldehyde for 20 min at room temperature (RT). Colonies were stained with 1 mL of 0.01% crystal violet for 15 min, rinsed three times with water, and air-dried. Colonies were counted using ImageJ software.

DNA damage by comet assay

DNA damage was assessed using the Comet assay kit (4250–050-K, R&D Systems) following the manufacturer's protocol. After treating cells with CBA and etoposide for 48 h, they were mixed with low-melting-point agarose (LMAgarose) and applied to Comet slides. Slides were pre-cooled at 4°C for 30 min, followed by overnight immersion in lysis solution at 4°C. The following day, the slides were unwound in alkaline unwinding solution for 1 h at 4°C, and electrophoresis was performed at 21 V for 40 min. After washing with dH_2O and dehydrating in 70% ethanol, the slides were air-dried in the dark for 30 min at RT. DNA was stained with SYBR Green (S33102, Invitrogen, CA, USA) for 30 min and observed under a microscope.

Please cite this article in press as: Jo et al., A natural compound derivative targeting HADHA disrupts mitochondrial homeostasis and suppresses renal cell carcinoma, Molecular Therapy (2026), https://doi.org/10.1016/j.ymthe.2026.10.014

DNA tail (%) and tail length (μm) were analyzed using ImageJ software.

Fluorescence-activated cell sorting

Apoptosis was measured using the Annexin V kit (sc-4252 AK, Santa Cruz, CA, USA) following the manufacturer's protocol. Cells were seeded into 12-well plates at a density of 2×10^4 cells/well and treated with CBA for 48 h. Afterward, cells were resuspended in 1× assay buffer and incubated with 5 μL of Annexin fluorescein isothiocyanate (FITC) for 15 min at RT. For cell cycle analysis, cells were treated with CBA and etoposide for 48 h, then fixed with 70% ethanol for 20 min on ice. After centrifugation, cells were washed with 1× PBS and stained with 1× propidium iodide (PI) solution for 15 min. Cells were analyzed by fluorescence-activated cell sorting (FACS; BD Biosciences, NJ, USA), and the data were processed using FlowJo software.

Measurement of intracellular ROS

Intracellular ROS levels were measured using the Cellular ROS Assay Kit (Red, ab186027, Abcam, Cambridge, UK) according to the manufacturer's instructions, with minor modifications. Briefly, cells were seeded in black-walled, clear-bottom 96-well plates and allowed to attach overnight. The next day, cells were pretreated with 25 μM z-VAD-FMK (HY-16658B, MedChemExpress, NJ, USA) for 1 h, followed by treatment with CBA in the continued presence or absence of z-VAD-FMK. Vehicle-treated cells were included as controls. ROS levels were measured at 2 and 6 h after CBA treatment. One hour before each endpoint, ROS Red dye working solution was added directly to the culture medium, and cells were incubated at 37°C protected from light. Fluorescence intensity was measured using a microplate reader at excitation and emission wavelengths of 520 and 605 nm, respectively. Background fluorescence from blank wells and no-dye control wells was subtracted from the raw fluorescence values. ROS levels were normalized to the vehicle-treated control and are presented as relative fluorescence intensity.

Transcriptomic analysis—RNA sequencing

Caki-1 and ACHN cells were cultured in 35 mm × 10 mm cell culture dishes and treated with 2 μM CBA for 24 h. RNA was extracted using QIAzol Lysis Reagent (79306, QIAGEN, MD, USA) and the RNeasy Kit (73404, QIAGEN, MD, USA). RNA quality and integrity were assessed with a Qubit 2.0 Fluorometer (Thermo Fisher Scientific, Waltham, MA, USA). RNA-seq libraries were prepared using the NEBNext Ultra II RNA Library Prep Kit (E6440S, New England Biolabs, Ipswich, MA, USA). Differential gene expression between control and treated samples was analyzed using a clustering algorithm applied to overlapping genes. A heatmap of gene expression was generated with the Euclidean distance and average linkage methods, using MeV 4.9.0 software. DEGs were further analyzed through the DAVID bioinformatics online tool (https://david.ncifcrf.gov/) for Gene Ontology and Kyoto Encyclopedia of Genes and Genomes (KEGG) pathway analysis. Protein-protein interaction (PPI) networks were identified using STRING and visualized in Cytoscape v.3.8.1. This analysis provides insights into the biological functions and pathways associated with the DEGs.

Immunofluorescence staining

Caki-1, ACHN, and HK-2 cells (1×10^5 cells) were seeded in 6-well plates and treated with CBA for 24 h. Cells were fixed and permeabilized using 4% paraformaldehyde and 0.1% Triton X-100. After blocking with 2% bovine serum albumin for 1 h, the cells were incubated with primary antibodies against γH2AX and TOM20 at 25°C for 3 h. The cells were then incubated with an FITC-conjugated secondary antibody for 30 min. Fluorescence images were captured using a Leica fluorescence microscope and analyzed with ImageJ software.

Animal ethics and biosafety statement

NSG mice were transferred from the Jackson Laboratories and housed and bred under the Duke Animal Care and Use program. The injection of cells was performed according to protocols approved by Duke's Animal Research Committee. All animal experiments were performed following protocols approved by Duke University.

Lentiviral vectors

Lentiviral vectors silencing HADHA were designed and constructed based on pLKO.1 puro (8453, Addgene, MA, USA) and tet-pLKO-puro (21916, Addgene, MA, USA). Lentiviral vectors overexpressing HADHA and HADHA with a 6× His-tag (HADHA-His) were designed and constructed based on the FUCGW (referred to as CGW) vector from Dr. Owen Witte at the University of California, Los Angeles. Lentiviral vectors were transfected into HEK293T cells together with pMDL, pVSVG, and pREV to make lentivirus. The sequences targeting shHADHA were as follows: shHADHA#1, 5′-CCTACAAAGGAGACAACTA-3′; and shHADHA#2, 5′-AGGAA-CAACCTCATTCTAA-3′. Plasmids with a scramble shRNA (47541, Addgene, MA, USA) (shSCR: 5′-CCTAAGGT-TAAGTCGCCCTCG-3′) were constructed and used as controls. HADHA cDNA was obtained from HEK293T.

Tumor induction in immunodeficient mouse model

Male 6- to 8-week-old NSG mice were purchased from Jackson Laboratory. Caki-1 and ACHN cells were mixed with Matrigel (356234, Corning Life Sciences, NY, USA), and 5×10^6 cells were injected subcutaneously into the mice. When tumor volume reached 100 mm^3, the mice were randomly divided into two groups. Tumors were treated with 50 mg/kg CBA every 2 days for a total of 7 treatments through i.p. injections. Tumor volume was calculated using the formula: volume = length × $width^2$ × 1/2.

Drug toxicity assessment

NSG mice after the 2-week treatment with CBA or DMSO were deeply anesthetized. Blood samples were drawn through cardiac puncture and submitted to Duke University's Division of Laboratory Animal Resources (DLAR), where the CBC and assessment of ALT and AST levels were performed using Heska ElementHT5 and DriChem. Reference values of parameters were retrieved from

Please cite this article in press as: Jo et al., A natural compound derivative targeting HADHA disrupts mitochondrial homeostasis and suppresses renal cell carcinoma, Molecular Therapy (2026), https://doi.org/10.1016/j.ymthe.2026.10.014

Jackson Laboratory and Layssol-Lamour et al.,[34] while the normal ranges were provided by DLAR. According to the Common Terminology Criteria for Adverse Events (CTCAE), the definitions of mild, moderate, and severe liver toxicity based on AST and ALT were referred to as 1–3 times the upper limit of normal (ULN), 3–5 times ULN, and more than 5 times ULN, respectively.

Histology and immunohistochemical staining

Tumor tissues were collected and immediately fixed in formalin. The tissues were then embedded in paraffin and sectioned to a thickness of 5 μm. The samples were used for hematoxylin and eosin (H&E) staining and IHC for γH2AX, cleaved PARP, p53, Ki67, and p-HH3. The percentage of positive staining was calculated using ImageJ software. The staining ratio (%) was determined as (positive area/total area) × 100.

Proteomic analyses

Two high-throughput proteomics approaches including SPROX and TPP were employed to identify proteins stabilized upon binding to CBA.[27,28] In the case of both techniques, previously established "one-pot" protocols were employed.[35–37] In TPP, proteins in Caki-1, ACHN, and HK-2 cell lysates were treated with either 1% DMSO (control) or 0.1 mM CBA, subjected to thermal denaturation at 37°C–64°C, and centrifuged to isolate stabilized proteins. In SPROX, proteins in Caki-1, ACHN, and HK-2 cell lysates were chemically denatured using a urea gradient (6–0.5 M) and subjected to H_2O_2-mediated oxidation reaction targeting methionine residues in proteins, before the reactions quenched to capture stability-dependent oxidation. Ultimately, the "one-pot" samples generated by each technique were submitted to a quantitative, bottom-up proteomics analysis using a 10-plex of tandem mass tags to facilitate multiplexed quantitative analysis via liquid chromatography-tandem mass spectrometry (LC-MS/MS). SPROX and TPP analyses of each cell line in the presence and absence of CBA were performed in pentaplicate, using a total of six TMT 10-plexes, according to a previously established workflow.[35] Protein hits in the TPP and SPROX experiments with a significant fold-change (p value <0.05) in the one-pot signals generated from the with and without ligand samples in each analysis were selected due to their ligand-induced stability. Together, TPP and SPROX provide complementary insights into protein-ligand interactions, enabling the identification of proteome-wide targets and the elucidation of mechanisms of action.

Cellular thermal shift assay

To assess the direct binding and thermal stability of HADHA upon drug treatment, a modified CETSA protocol was performed. Cells were treated with 0.2 μM CBA or an equal volume of vehicle (DMSO) for 3 h in 10-cm culture dishes. Following treatment, cells were harvested, pelleted, and resuspended in 500 μL of cold PBS containing protease inhibitors. The suspension was aliquoted into eight PCR tubes (50 μL each) for the temperature gradient samples, and an additional 50 μL aliquot was placed in a 1.7-mL tube for the RT control. Samples were kept on ice prior to heating. The thermal denaturation step was performed using a thermocycler, heating samples for 3 min at increasing temperatures ranging from 42°C to 50°C. The RT control was incubated at room temperature for 3 min. After heating, the samples were immediately placed on dry ice for 10 min, followed by incubation at 37°C for 10 min to complete one freeze-thaw cycle. This process was repeated three times to facilitate complete lysis. Samples were briefly centrifuged to collect condensate, transferred to 1.7-mL tubes, and centrifuged at 14,000 × g for 20 min at 4°C to separate soluble and aggregated protein fractions. The supernatant containing soluble protein was mixed with 5× SDS sample buffer, heated at 95°C for 10 min, and analyzed by SDS-PAGE followed by immunoblotting. Protein samples were loaded from the lowest to the highest temperature to evaluate HADHA thermal stability under each condition.

Purification of recombinant HADHA protein

HEK293T cells were transduced to express HADHA-His. 3 × 10^9 cells were harvested in buffer containing 1% Triton X-100, 300 mM NaCl, 20 mM Tris-HCl (pH 7.5), 10% glycerol, 20 mM imidazole, and protease inhibitor (11836170001, Roche, IN, USA). Lysate was sonicated and centrifuged at 20,000 × g, 4°C for 10 min. Supernatant was incubated with Ni-NTA beads (PI88221, Thermo Fisher Scientific, Waltham, MA, USA) at 4°C for 2 h. Beads were harvested and washed with a buffer containing 300 mM NaCl, 20 mM Tris-HCl (pH 7.5), and 20 mM imidazole and eluted in buffer containing 0.5% Tween 20, 300 mM NaCl, 20 mM Tris-HCl (pH 7.5), and 500 mM imidazole. 10 kDa centrifugal filter (UFC9010, Merck/Sigma-Aldrich, St. Louis, MO, USA) was applied to concentrate the protein and dilute imidazole.

Thermal shift assay using purified HADHA

Thermal shift assays were performed using purified recombinant HADHA protein to assess CBA-induced thermal stabilization. For the differential scanning fluorimetry assay, 1 μg purified HADHA was incubated with vehicle or the indicated concentrations of CBA in assay buffer for 15 min at RT. Protein thermal stability was monitored across a temperature gradient from 25°C to 99°C, using Protein Thermal Shift Dye Kit (4461146, Thermo Fisher Scientific, Waltham, MA, USA) and ViiA 7 Real-Time PCR System (Applied Biosystems, Thermo Fisher Scientific, Waltham, MA, USA). Fluorescence signals were recorded during thermal denaturation, and Tm were calculated by fitting the melting curves. ΔTm values were calculated by subtracting the Tm of the vehicle-treated control from the Tm of the CBA-treated samples. For the thermal shift assay followed by immunoblotting, 5 μg purified HADHA was incubated with 0.2 mM CBA or vehicle in a buffer containing 300 mM NaCl and 20 mM Tris-HCl (pH 7.5) at RT for 15 min, then aliquoted and subjected to 3-min incubation at temperatures ranging from 25°C to 61°C. Samples were centrifuged at 20,000 × g at 4°C for 20 min. Supernatants were taken for immunoblotting.

Live-cell imaging

The growth and viability of the cultures were monitored with the live-cell imaging system IncucyteR S3 (Sartorius, Germany). Phase-contrast images were acquired every 4 h up to 48 h.

Please cite this article in press as: Jo et al., A natural compound derivative targeting HADHA disrupts mitochondrial homeostasis and suppresses renal cell carcinoma, Molecular Therapy (2026), https://doi.org/10.1016/j.ymthe.2026.10.014

Immunoblotting

To test the effect of CBA, 1×10^6 cells were treated for 24 h prior to harvest. To test the effect of HADHA knockdown, 2.5×10^5 cells were lentivirally transduced with shHADHA for 5 days prior to harvest. For the inducible knockdown system, 2.5×10^5 cells from the established tet-shHADHA cell lines were treated with 1 μg/mL Dox for 5 days prior to harvest. Cells were lysed in 9 M urea buffer with 4% CHAPS and protease inhibitor (35976600, Roche, IN, USA). SDS-PAGE gel electrophoresis was performed, and protein transfer was performed onto a nitrocellulose membrane (84–876, Genesee Scientific, CA, USA). Membranes were incubated with primary antibodies at 4°C overnight, then with secondary antibodies at room temperature for 2 h. Protein detection was performed using ECL reagent (20-300B, Genesee Scientific, CA, USA) and captured on a Prosignal blotting film (30-507L, Genesee Scientific, CA, USA).

Fatty acid oxidation assay

FAO activity was measured using the FAO-Glo Fatty Acid Oxidation Assay (CS3271A08, Promega, Madison, WI, USA) according to the manufacturer's instructions, with minor modifications. Briefly, Caki-1 and ACHN cells were seeded in 96-well plates and allowed to attach overnight. For CBA treatment experiments, cells were treated with DMSO or CBA at the indicated concentrations. For inducible HADHA knockdown experiments, tet-shSCR and tet-shHADHA cells were treated with Dox to induce shRNA expression. After treatment, FAO substrate was added to live cells, and cells were incubated at 37°C for the indicated time. FAO Luciferin Detection Reagent was then added, and luminescence was measured using a microplate reader. In parallel wells, cell viability was measured using CellTiter-Glo (G9241, Promega, WI, USA) to normalize FAO activity to viable cell number. Relative FAO activity was calculated by subtracting background luminescence and normalizing FAO-Glo luminescence to the corresponding viability signal and vehicle or control group.

Acetyl-CoA assay

Cellular acetyl-CoA levels were measured using the Acetyl Coenzyme A Assay Kit (MAK566, Merck/Sigma-Aldrich, St. Louis, MO, USA) according to the manufacturer's protocol. Briefly, cells were treated with DMSO or CBA, or tet-shSCR and tet-shHADHA cells were treated with Dox to induce HADHA knockdown. Cell pellets were collected, washed with cold PBS, and stored at −80°C until analysis. Frozen pellets were extracted and deproteinized using perchloric acid, followed by neutralization with potassium bicarbonate. Insoluble material was removed by centrifugation, and the clarified supernatants were used for acetyl-CoA measurement. Samples and acetyl-CoA standards were loaded into black 96-well plates in technical duplicates. Reaction mixture and reaction initiator solution were added according to the manufacturer's instructions, and fluorescence was measured at excitation/emission wavelengths of 340/460 nm using a microplate reader. Acetyl-CoA levels were calculated from a standard curve after background subtraction and normalized to cell number or protein content.

Data analysis

All experiments were performed in triplicate, and data are expressed as the mean ± standard deviation. Statistical comparisons between two groups were performed using Student's t test, with significance defined as *: $p < 0.05$, **: $p < 0.01$, ***: $p < 0.001$, and ****: $p < 0.0001$. Statistical comparisons of multiple groups were performed using ANOVA followed by Dunnett's multiple-comparison test, with significance defined as *: $p < 0.05$, **: $p < 0.01$, ***: $p < 0.001$, and ****: $p < 0.0001$.

DATA AND CODE AVAILABILITY

The RNA-seq dataset has been deposited in the Gene Expression Omnibus (GEO) and is accessible with accession number GEO: GSE302865. The proteomic dataset has been deposited in the ProteomeXchange/PRIDE database, with accession number ProteomeXchange: PXD080542.

ACKNOWLEDGMENTS

This research was supported by the Rollie Endowed Assistant Professorship (J.W.P.) at Duke University.

AUTHOR CONTRIBUTIONS

A.J., M.C.F., J. Hong, and J.W.P. conceptualized and designed the study; A.J., S.D., H. Jung, Z.W., M.A.B., H.-J.P., M.C.F., J. Hong, and J.W.P. analyzed the data and helped prepare the manuscript; S.D. and J.W.P. wrote the draft of this manuscript; A.J., A.T., B.T., J.M., Z.Y., J.L., and J.W.P. performed bioinformatic analyses, data curation, and methodology; J.P. and J. Hong synthesized and provided the CBA compound; M.A.B., V.M.M., and H.-J.P. performed proteomic analyses; J. Huang and D.H. evaluated the histology of RCC xenograft tissues; D.W., K.C., N.C., and Y.J. assisted and supported the experiments; K.S. provided RCC cell lines; M.C.F., J. Hong, and J.W.P. supervised the study and secured funding for it. All authors read, commented on, and approved this manuscript.

DECLARATION OF INTERESTS

J. Huang is a consultant for or owns shares in the following companies: Artera, Kingmed Diagnostics, MoreHealth, OptraScan, York Biotechnology, Chimigen Bio, and Sisu Pharma. A.A. reports research support (to Duke) from the NIH/NCI, PCF, DOD, Astellas, Pfizer, Bayer, Janssen, BMS, AstraZeneca, Merck, Pathos, Amgen, Novartis, and Fibrogen; he reports consulting or advising relationships with Astellas, Pfizer, Bayer, Janssen, BMS, AstraZeneca, Merck, Exelixis, Novartis, Medscape, Telix, Duality Bio, MedIQ, IDEOlogy, Sumitomo, and Precede Bio.

SUPPLEMENTAL INFORMATION

Supplemental information can be found online at https://doi.org/10.1016/j.ymthe.2026.10.014.

REFERENCES

1. Adhikari, A., Sapkota, S., Gogia, S., and Kc, O. (2024). Changes in the overall survival of patients with metastatic renal cell carcinoma in the era of immune-checkpoint inhibitors. Cancer Epidemiol. *92*, 102639. https://doi.org/10.1016/j.canep.2024.102639.

2. Jammihal, T., Saliby, R.M., Labaki, C., Soulati, H., Gallegos, J., Peris, A., McCurry, D., Yu, C., Shah, V., Poduval, D., et al. (2025). Immunogenomic determinants of exceptional response to immune checkpoint inhibition in renal cell carcinoma. Nat. Cancer *6*, 372–384. https://doi.org/10.1038/s43018-024-00896-w.

3. Atkins, M.B., and Choueiri, T.K. (2016). Epidemiology, pathology, and pathogenesis of renal cell carcinoma. UpToDate.

4. Quinn, A.E., Bell, S.D., Marrah, A.J., Wakefield, M.R., and Fang, Y. (2024). The current state of the diagnoses and treatments for clear cell renal cell carcinoma. Cancers *16*, 4034. https://doi.org/10.3390/cancers16234034.

Please cite this article in press as: Jo et al., A natural compound derivative targeting HADHA disrupts mitochondrial homeostasis and suppresses renal cell carcinoma, Molecular Therapy (2026), https://doi.org/10.1016/j.ymthe.2026.10.014

5. Jiang, A., Li, J., He, Z., Liu, Y., Qiao, K., Fang, Y., Qu, L., Luo, P., Lin, A., and Wang, L. (2024). Renal cancer: signaling pathways and advances in targeted therapies. MedComm *5*, e676. https://doi.org/10.1002/mco2.676.

6. Ernst, M.S., Navani, V., Wells, J.C., Donskov, F., Basappa, N., Labaki, C., Pal, S.K., Meza, L., Wood, L.A., Ernst, D.S., et al. (2023). Outcomes for international metastatic renal cell carcinoma database consortium prognostic groups in contemporary first-line combination therapies for metastatic renal cell carcinoma. Eur. Urol. *84*, 109–116. https://doi.org/10.1016/j.eururo.2023.01.001.

7. Yip, S.M., Wells, C., Moreira, R., Wong, A., Srinivas, S., Beuselinck, B., Porta, C., Sim, H.W., Ernst, D.S., Rini, B.I., et al. (2018). Checkpoint inhibitors in patients with metastatic renal cell carcinoma: results from the international metastatic renal cell carcinoma database consortium. Cancer *124*, 3677–3683. https://doi.org/10.1002/cncr.31595.

8. Navani, V., and Heng, D.Y.C. (2022). Treatment selection in first-line metastatic renal cell carcinoma—the contemporary treatment paradigm in the age of combination therapy: a review. JAMA Oncol. *8*, 292–299. https://doi.org/10.1001/jamaoncol.2021.4337.

9. Ingels, A., Campi, R., Capitanio, U., Amparore, D., Bertolo, R., Carbonara, U., Erdem, S., Kara, Ö., Klatte, T., Kriegmair, M.C., et al. (2022). Complementary roles of surgery and systemic treatment in clear cell renal cell carcinoma. Nat. Rev. Urol. *19*, 391–418. https://doi.org/10.1038/s41585-022-00592-3.

10. Roskoski, R., Jr. (2024). Combination immune checkpoint and targeted protein kinase inhibitors for the treatment of renal cell carcinomas. Pharmacol. Res. *203*, 107181. https://doi.org/10.1016/j.phrs.2024.107181.

11. Zhu, Z., Jin, Y., Zhou, J., Chen, F., Chen, M., Gao, Z., Hu, L., Xuan, J., Li, X., Song, Z., and Guo, X. (2024). PD1/PD-L1 blockade in clear cell renal cell carcinoma: mechanistic insights, clinical efficacy, and future perspectives. Mol. Cancer *23*, 146. https://doi.org/10.1186/s12943-024-02059-y.

12. Rosellini, M., Marchetti, A., Mollica, V., Rizzo, A., Santoni, M., and Massari, F. (2023). Prognostic and predictive biomarkers for immunotherapy in advanced renal cell carcinoma. Nat. Rev. Urol. *20*, 133–157. https://doi.org/10.1038/s41585-022-00676-0.

13. Chunarkar-Patil, P., Kaleem, M., Mishra, R., Ray, S., Ahmad, A., Verma, D., Bhayye, S., Dubey, R., Singh, H.N., and Kumar, S. (2024). Anticancer drug discovery based on natural products: from computational approaches to clinical studies. Biomedicines *12*, 201. https://doi.org/10.3390/biomedicines12010201.

14. Rui, S., Fengrui, G., Yining, Z., Hong, S., Xuewen, Y., Changping, W., and Chunjia, Y. (2025). Biological activity of secondary metabolites of actinomycetes and their potential sources as antineoplastic drugs: a review. Front. Microbiol. *16*, 1550516. https://doi.org/10.3389/fmicb.2025.1550516.

15. Giurini, E.F., Godla, A., and Gupta, K.H. (2024). Redefining bioactive small molecules from microbial metabolites as revolutionary anticancer agents. Cancer Gene Ther. *31*, 187–206. https://doi.org/10.1038/s41417-023-00715-x.

16. Engelbrecht, A., Saad, H., Gross, H., and Kaysser, L. (2021). Natural products from Nocardia and their role in pathogenicity. Microb. Physiol. *31*, 217–232. https://doi.org/10.1159/000516864.

17. Xuan, J., Chen, S., Ning, B., Tolleson, W.H., and Guo, L. (2016). Development of HepG2-derived cells expressing cytochrome P450s for assessing metabolism-associated drug-induced liver toxicity. Chem. Biol. Interact. *255*, 63–73. https://doi.org/10.1016/j.cbi.2015.10.009.

18. Brix, N., Samaga, D., Belka, C., Zitzelsberger, H., and Lauber, K. (2021). Analysis of clonogenic growth in vitro. Nat. Protoc. *16*, 4963–4991. https://doi.org/10.1038/s41596-021-00615-0.

19. Slee, E.A., Zhu, H., Chow, S.C., MacFarlane, M., Nicholson, D.W., and Cohen, G.M. (1996). Benzyloxycarbonyl-Val-Ala-Asp (OMe) fluoromethylketone (Z-VAD.FMK) inhibits apoptosis by blocking the processing of CPP32. Biochem. J. *315*, 21–24. https://doi.org/10.1042/bj3150021.

20. Tarsounas, M., Davies, A.A., and West, S.C. (2004). RAD51 localization and activation following DNA damage. Philos. Trans. R. Soc. Lond. B Biol. Sci. *359*, 87–93. https://doi.org/10.1098/rstb.2003.1368.

21. Clutton, G., Mollan, K., Hudgens, M., and Goonetilleke, N. (2019). A reproducible, objective method using MitoTracker® fluorescent dyes to assess mitochondrial mass in T cells by flow cytometry. Cytometry. A. *95*, 450–456. https://doi.org/10.1002/cyto.a.23705.

22. Endo, T., and Wiedemann, N. (2025). Molecular machineries and pathways of mitochondrial protein transport. Nat. Rev. Mol. Cell Biol. *26*, 848–867. https://doi.org/10.1038/s41580-025-00865-w.

23. Detmer, S.A., and Chan, D.C. (2007). Functions and dysfunctions of mitochondrial dynamics. Nat. Rev. Mol. Cell Biol. *8*, 870–879. https://doi.org/10.1038/nrm2275.

24. Taguchi, N., Ishihara, N., Jofuku, A., Oka, T., and Mihara, K. (2007). Mitotic phosphorylation of dynamin-related GTPase Drp1 participates in mitochondrial fission. J. Biol. Chem. *282*, 11521–11529. https://doi.org/10.1074/jbc.M607279200.

25. Chen, H., Detmer, S.A., Ewald, A.J., Griffin, E.E., Fraser, S.E., and Chan, D.C. (2003). Mitofusins Mfn1 and Mfn2 coordinately regulate mitochondrial fusion and are essential for embryonic development. J. Cell Biol. *160*, 189–200. https://doi.org/10.1083/jcb.200211046.

26. Frezza, C., Cipolat, S., Martins de Brito, O., Micaroni, M., Beznoussenko, G.V., Rudka, T., Bartoli, D., Polishuck, R.S., Danial, N.N., De Strooper, B., and Scorrano, L. (2006). OPA1 controls apoptotic cristae remodeling independently from mitochondrial fusion. Cell *126*, 177–189. https://doi.org/10.1016/j.cell.2006.06.025.

27. West, G.M., Tang, L., and Fitzgerald, M.C. (2008). Thermodynamic analysis of protein stability and ligand binding using a chemical modification-and mass spectrometry-based strategy. Anal. Chem. *80*, 4175–4185. https://doi.org/10.1021/ac702610a.

28. Savitski, M.M., Reinhard, F.B.M., Franken, H., Werner, T., Savitski, M.F., Eberhard, D., Martinez Molina, D., Jafari, R., Dovega, R.B., Klaeger, S., et al. (2014). Tracking cancer drugs in living cells by thermal profiling of the proteome. Science *346*, 1255784. https://doi.org/10.1126/science.1255784.

29. Pan, A., Sun, X.-M., Huang, F.-Q., Liu, J.-F., Cai, Y.-Y., Wu, X., Alolga, R.N., Li, P., Liu, B.-L., Liu, Q., and Qi, L.W. (2022). The mitochondrial β-oxidation enzyme HADHA restrains hepatic glucagon response by promoting β-hydroxybutyrate production. Nat. Commun. *13*, 386. https://doi.org/10.1038/s41467-022-28044-x.

30. Chi, Z., Chen, S., Xu, T., Zhen, W., Yu, W., Jiang, D., Guo, X., Wang, Z., Zhang, K., Li, M., et al. (2020). Histone deacetylase 3 couples mitochondria to drive IL-1β-dependent inflammation by configuring fatty acid oxidation. Mol. Cell *80*, 43–58.e7. https://doi.org/10.1016/j.molcel.2020.08.015.

31. Liu, S., Liu, X., Wu, F., Zhang, X., Zhang, H., Gao, D., Bi, D., Qu, H., Ge, J., Xu, Y., and Zhao, Z. (2019). HADHA overexpression disrupts lipid metabolism and inhibits tumor growth in clear cell renal cell carcinoma. Exp. Cell Res. *384*, 111558. https://doi.org/10.1016/j.yexcr.2019.111558.

32. Chakraborty, S., Balan, M., Sabarwal, A., Choueiri, T.K., and Pal, S. (2021). Metabolic reprogramming in renal cancer: Events of a metabolic disease. Biochim. Biophys. Acta Rev. Cancer *1876*, 188559. https://doi.org/10.1016/j.bbcan.2021.188559.

33. Zois, C.E., and Harris, A.L. (2016). Glycogen metabolism has a key role in the cancer microenvironment and provides new targets for cancer therapy. J. Mol. Med. *94*, 137–154. https://doi.org/10.1007/s00109-015-1377-9.

34. Layssol-Lamour, C.J., Sarry, J.E., Braun, J.P.D., Trumel, C., and Bourgès-Abella, N.H. (2021). Reference Values for Hematology, Plasma Biochemistry, Bone Marrow Cytology and Bone Histology of NOD.Cg-Prkdc(scid) Il2rg(tm1Wjl)/SzJ Immunodeficient Mice. J. Am. Assoc. Lab. Anim. Sci. *60*, 4–17. https://doi.org/10.30802/AALAS-JAALAS-20-000020.

35. Cabrera, A., Wiebelhaus, N., Quan, B., Ma, R., Meng, H., and Fitzgerald, M.C. (2020). Comparative analysis of mass-spectrometry-based proteomic methods for protein target discovery using a one-pot approach. J. Am. Soc. Mass Spectrom. *31*, 217–226. https://doi.org/10.1021/jasms.9b00041.

36. Gaetani, M., Sabatier, P., Saei, A.A., Beusch, C.M., Yang, Z., Lundström, S.L., and Zubarev, R.A. (2019). Proteome integral solubility alteration: a high-throughput proteomics assay for target deconvolution. J. Proteome Res. *18*, 4027–4037. https://doi.org/10.1021/acs.jproteome.9b00500.

37. Liu, Y.-K., Chen, H.-Y., Chueh, P.J., and Liu, P.-F. (2019). A one-pot analysis approach to simplify measurements of protein stability and folding kinetics. Biochim. Biophys. Acta Proteins Proteom. *1867*, 184–193. https://doi.org/10.1016/j.bbapap.2018.12.006.